Tectono-Sedimentary Evolution of Shale-Related Minibasins in the Karvandar Basin (South Sistan, SE Iran): Insights From Magnetostratigraphy, Isotopic Dating, and Sandstone Petrology

Journal Article

Author(s):
Ruh, Jonas Bruno; Valero, Luis; Najafi, Mohammad; Etemad-Saeed, Najmeh; Vouga, J.; Mohammadi, Ali; Landtwing, Fabio; Guillong, Marcel; Cobianchi, Miriam; Mancin, Nicoletta

Publication date:
2023-11

Permanent link:
https://doi.org/10.3929/ethz-b-000641503

Originally published in:
Tectonics 42(11), https://doi.org/10.1029/2023TC007971

Tectonics®

RESEARCH ARTICLE
10.1029/2023TC007971

Key Points:

- A ~3.5-km-thick section in the Karvandar foreland basin was sampled for magnetostratigraphy and sandstone framework analysis
- The shallow-marine to continental sequence (24–18 Ma) consists of first-cycle volcanic lithics and overlays an olistostrome deposit
- The late Oligocene to early Miocene sequence represents the erosion product of a volcanic arc related to the Makran subduction

Supporting Information:

Supporting Information may be found in the online version of this article.

Correspondence to:

J. B. Ruh,
jruh@icm.csic.es

Citation:

Ruh, J. B., Valero, L., Najafi, M., Etemad-Saeed, N., Vouga, J., Mohammadi, A., et al. (2023). Tectono-sedimentary evolution of shale-related minibasins in the Karvandar Basin (South Sistan, SE Iran): Insights from magnetostratigraphy, isotopic dating, and sandstone petrology. *Tectonics*, *42*, e2023TC007971. https://doi.org/10.1029/2023TC007971

Received 15 JUN 2023
Accepted 12 OCT 2023

Author Contributions:

Conceptualization: J. B. Ruh, L. Valero, M. Najafi, A. Mohammadi
Formal analysis: J. B. Ruh, L. Valero, N. Etemad-Saeed, J. Vouga, F. Landtwing, M. Guillong, M. Cobianchi, N. Mancin
Investigation: J. B. Ruh, L. Valero, M. Najafi, N. Etemad-Saeed, A. Mohammadi, F. Landtwing, M. Cobianchi, N. Mancin
Methodology: M. Guillong
Project Administration: J. B. Ruh
Resources: J. B. Ruh, L. Valero

Tectono-Sedimentary Evolution of Shale-Related Minibasins in the Karvandar Basin (South Sistan, SE Iran): Insights From Magnetostratigraphy, Isotopic Dating, and Sandstone Petrology

J. B. Ruh[1,2], L. Valero[3], M. Najafi[4,5], N. Etemad-Saeed[6,7], J. Vouga[2], A. Mohammadi[8], F. Landtwing[2], M. Guillong[2], M. Cobianchi[9], and N. Mancin[9]

[1]Institute of Marine Sciences, Consejo Superior de Investigaciones Científicas, Barcelona, Spain, [2]Structural Geology and Tectonics, Geological Institute, Department of Earth Science, ETH Zürich, Zürich, Switzerland, [3]Departament de Dinàmica de la Terra i de l'Oceà and Institut de Recerca Geomodels, Universitat de Barcelona, Barcelona, Spain, [4]Tarbiat Modares University, Teheran, Iran, [5]Geosciences Barcelona, CSIC, Barcelona, Spain, [6]Department of Earth Sciences, Institute for Advanced Studies in Basic Sciences (IASBS), Zanjan, Iran, [7]Department of Earth, Atmospheric and Planetary Sciences, Massachusetts Institute of Technology, Cambridge, MA, USA, [8]Eurasia Institute of Earth Sciences, Istanbul Technical University, Istanbul, Turkey, [9]Department of Earth and Environmental Sciences, University of Pavia, Pavia, Italy

Abstract Sediments deposited into foreland basins can provide valuable insights related to the geological evolution of their hinterlands. Located in the peripheral foreland of the South Sistan Suture Zone (SE Iran), the Karvandar Basin exhibits a several-kilometer-thick shallow-marine to continental clastic sedimentary sequence forming elongated sub-circular synclines. These synclines overlie a mud-dominated formation with exotic volcanic blocks that hosts one of Iran's largest mud volcano, known as Pirgel. In this study, we present a ~3.5-km-thick magnetostratigraphic section and U-Pb zircon ages of interlayered tuffs that constrain a depositional age of the Karvandar Basin of ~24–17 Ma. Sandstone and microconglomerate framework analyses and paleocurrent directions suggest a first-cycle active volcanic arc source to the northeast of the basin. We interpret the mud-dominated lithology with volcanic blocks as an olistostrome originating from a similar source as the overlying clastic sequence. The deposition of the olistostrome is dated at ~24.5 Ma by a U-Pb calcite age from a coral block. The absence of large-scale anticlines and the occurrence of angular unconformities suggest that the sub-circular synclines in the Karvandar Basin formed by gravity-driven downbuilding into the unconsolidated fluid-saturated olistostrome, resembling salt-related minibasins. Integrated results indicate that a late Oligocene to early Miocene Makran volcanic arc represents the source of the clastic sequence. Hence, our results provide new constraints on the initiation of arc volcanism related to the Makran subduction zone, predating earliest reported ages from the Mirabad pluton (19 Ma) to the northeast of the Karvandar Basin by ~5 Myr.

1. Introduction

A foreland basin is a structural basin that develops in close proximity to an orogen as a result of continental collision and the subsequent flexure of the lithosphere due to the load of the uplifting mountain range (Allen & Homewood, 2009; DeCelles & Giles, 1996). Foreland basins can form on both the downgoing (peripheral) and overriding (retroarc) continental plates and usually consist of a thick sequence of clastic rocks, which are the erosion product of the adjacent mountain range. In the early stages of peripheral foreland basin stratigraphy, submarine turbiditic trench fill sediments (flysch) are often present, while later stages represent an overfilled basin with a shallow-marine or continental (molasse) depositional environment (Allen et al., 1991; Garcés et al., 2020). Various processes have been detected to potentially be accountable for the transition from a flysch-type (underfilled) to a molasse-type (overfilled) peripheral foreland basin. These include (a) the underthrusting of a progressively thickening passive margin and consequent uplift (i.e., shallowing) of the basin (Stockmal et al., 1986), (b) the increase of elastic thickness of the downgoing plate, which strengthens its flexural rigidity (Watts, 1992), and (c) slab breakoff resulting in isostatic rebound and uplift of the orogenic core linked to increased erosion rates that lead to overfilling of the foreland basin (Schlunegger & Castelltort, 2016; Sinclair, 1997). Moreover, interaction of climate change and regional tectonics could increase sediment fluxes leading to basin overfilling, as documented from the eastern South-Alpine foreland system during the Pleistocene (Mancin et al., 2009).

Supervision: J. B. Ruh, L. Valero, M. Najafi
Visualization: J. B. Ruh, N. Etemad-Saeed
Writing – original draft: J. B. Ruh
Writing – review & editing: L. Valero, M. Najafi, N. Etemad-Saeed, A. Mohammadi, M. Guillong, M. Cobianchi, N. Mancin

Nevertheless, tectonostratigraphic and sedimentological analyses from the Swiss Molasse basin demonstrated that tectonic processes, reduced sediment influx, and climate-induced sea level rise may result in regional transgression and flooding of a previously overfilled foreland (Garefalakis & Schlunegger, 2019). In particular, slab rollback was proposed to be responsible for the generation of additional accommodation space along the northern margin of the European Alps, besides topographic loading, explaining the inconsistencies between age constraints for the Molasse stratigraphy and paleoaltimetry estimates of the Alps (Dal Zilio et al., 2020; Schlunegger & Kissling, 2015).

Lithostratigraphic, chronostratigraphic, sedimentological, and petrological data of foreland basin deposits provide invaluable information for understanding the tectonic evolution of adjacent mountain ranges (e.g., Carrapa et al., 2016; Chapman et al., 2020). For example, variations in detrital petrography allows drawing conclusions about the exhumation of sedimentary and basement terrains in the hinterland (Etemad-Saeed et al., 2020; Schlunegger et al., 1998) and transitions in sedimentary provenance (DeCelles et al., 2004; Mohammadi, Kaveh-Firouz, et al., 2023). Additionally, low-temperature geochronology on detrital zircons and apatites in foreland deposits can provide insights into the exhumation paths of internal tectonic units that were exposed in the past (Najman et al., 2005; Spiegel et al., 2000; van der Beek et al., 2006). When combined with a precise chronological control on the stratigraphic record, obtained through integrated biostratigraphy, radiometric dating and magnetostratigraphy, foreland deposits allow for a detailed reconstruction of the geological history of the surrounding region (Carrapa et al., 2016; Chapman et al., 2020; Lease et al., 2012; Mancin et al., 2016; Schlunegger et al., 1997; Wang et al., 2022).

In this study, we apply magnetostratigraphy and sandstone framework analysis to a 3.5-km-thick Tertiary sequence of the Karvandar Basin, located near the Lut and Afghan/Helmand blocks and the Makran-Sistan triple junction (Figure 1). The geodynamic setting that led to the formation of this local basin remains unclear and three hypotheses have been proposed: (a) It represents a pull-apart basin related to strike-slip faulting along the East Lut Fault system, active since the Paleocene (Aghanabati et al., 1994; Bagheri & Damani Gol, 2020). (b) It represents, together with the Jaz-Murian Depression (the recent forearc basin of the Makran subduction zone), the eastern extension of the survival of a shallow sea inland of the Mesozoic ophiolite tract along the SE Zagros and the Makran subduction zone (McCall, 1997). (c) The Karvandar Basin represents a post-collisional peripheral foredeep basin of the South Sistan Suture Zone (SSZ) (Davoudzadeh, 1997).

The obtained magnetostratigraphy of the Karvandar Basin is correlated to the geomagnetic polarity timescale (GPTS), supported by the polarity-reversal pattern, with the assistance of U-Pb dating of three tuff layers and one coral sample. To examine the source areas of the sediments, the sandstone framework of 69 clastic samples along the same section is analyzed. This multidisciplinary approach not only provides a precise time constraint for the deposition of the predominantly continental sequence, but also allows for a reconstruction of the composition of the exhumed hinterland during the sediment accumulation period. We compare our results to previously published data related to the closure of the South Sistan Basin and the Makran subduction zone to gain new insight on the formation of the Karvandar Basin and the complex tectonic evolution of the region.

2. Geotectonic Setting

The Cenozoic Karvandar Basin (also known as Kaskin Basin in some publications; e.g., Bagheri & Damani Gol, 2020; Davoudzadeh, 1997; Huber, 1978; Mohammadi, Burg, & Winkler, 2016; Sahandi, 1996) is situated at the intersection of the SSZ and the Makran accretionary wedge (Figure 1a). This intersection represents the junction of the continental Lut and Afghan/Helmand blocks in the west and the east, respectively, and the northern extent of the Makran accretionary wedge in the south (hereafter called Makran-Sistan triple junction). The tectonic history of this region began after the separation of Central Iran (Yazd, Tabas, and Lut blocks), the Afghan/Helmand block, and the Sanandaj-Sirjan and Bajgan-Durkan blocks from the edge of Gondwana during the Permian and no later than Early Triassic (Burg, 2018; Senghor et al., 1988; Sudi Ajirlu et al., 2016), resulting in the formation of the Neo-Tethys Ocean (Muttoni et al., 2009). During the Late Jurassic and Early Cretaceous, several smaller oceans connected to the Neo-Tethys formed, partially as backarc basins resulting from the northward subduction of the Neo-Tethys (Hunziker et al., 2015; Lechmann et al., 2018; Moghadam et al., 2009; Mohammadi, Burg, & Guillong, 2022; Mohammadi, Ruh, et al., 2022; Rossetti et al., 2010). In the Late Cretaceous, the plate tectonic configuration resembled the present-day Mediterranean region, with multiple microcontinents separated by smaller branches of the Neo-Tethys (Nain-Baft, Fannuj, Sistan, Sabsevar, and Khoy oceans)

10.1029/2023TC007971

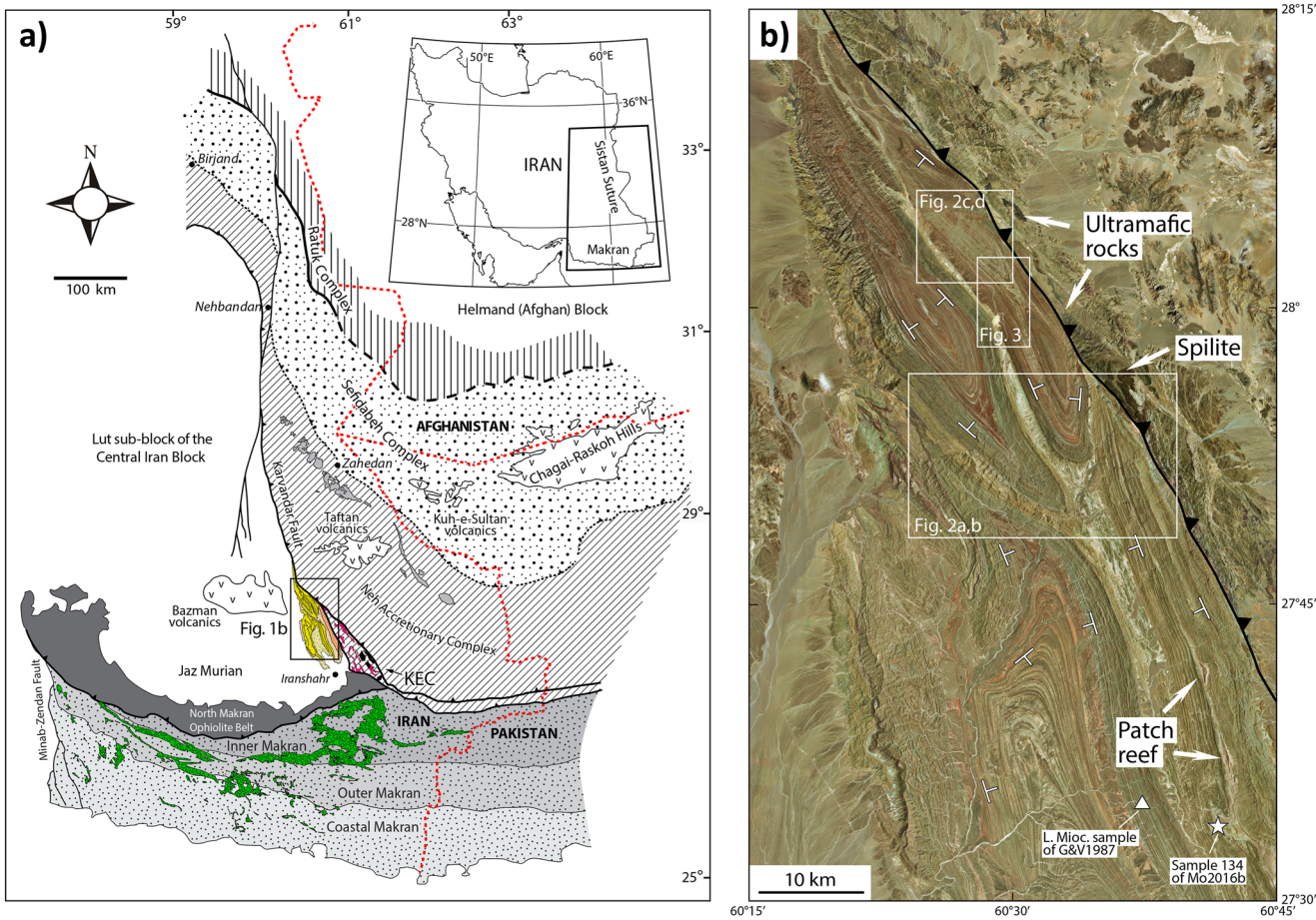

Figure 1. Geology of southeast Iran. (a) Tectono-stratigraphic setting of the ~N-S-trending South Sistan Basin (white patterns; modified from Mohammadi, Burg, and Winkler (2016)) and the W-E-trending Makran Accretionary Wedge (gray patterns; modified from Burg (2018)). The Bazman, Taftan and Kuh-e-Sultan volcanics represent the recent magmatic arc of the Makran subduction zone. Yellow colors indicate the Tertiary Karvandar Basin. Pink colors denote volcanic and ultrabasic slivers of the Karvandar Exotic Complex. Green colors illustrate exposures of the Tortonian olistrostrome in the Makran (Burg et al., 2008). Red dashed lines: Country borders. (b) Satellite image shows the Karvandar Basin with NNW-SSE-trending elongated, sub-circular synclines, bounded by the Karvandar Fault in the east. Study area outlined in panel (a). Star: Detrital zircon sample location of Mohammadi et al. (2016b). Triangle: Fossil sample location of Ghorashi and Vaezipour (1987).

surrounding the Central Iranian Blocks and the main Neo-Tethys Ocean to the south (McCall, 1997). The SSZ and the Makran accretionary wedge formed as a result of the (in the case of the Makran still ongoing) closure of different branches of the Neo-Tethys Ocean that initiated during the Cretaceous (e.g., Alavi, 2007; F. Berberian et al., 1982; Ricou, 1994).

2.1. Sistan Suture Zone

The roughly N-S-trending SSZ results from the closure of the Sistan Ocean and the subsequent collision between the Lut and the Afghan/Helmand blocks (Bagheri & Damani Gol, 2020; Bröcker et al., 2022; Tirrul et al., 1983). Biostratigraphy of radiolarites overlying the ophiolitic sequence and U-Pb ages of ophiolite-related leucogabbros indicate that the Sistan Ocean already existed in the Early Cretaceous (Babazadeh & De Wever, 2004; Zarrinkoub et al., 2012). Structural, petrological, and sedimentological studies suggest that the Sistan Ocean was subducting eastward beneath the Afghan/Helmand Block during Late Cretaceous (Angiboust et al., 2013; Bröcker et al., 2013; Jentzer et al., 2022; Mohammadi, Burg, Bouilhol, & Ruh, 2016; Mohammadi, Burg, et al., 2023). However, some studies interpret subduction vergence to be westward or double-sided, based on geochemical analyses of magmatic rocks from the Lut Block (e.g., Arjmandzadeh et al., 2011; Beydokhti et al., 2015; Pang et al., 2013). Continental collision of the Lut and Afghan/Helmand blocks in the North Sistan was proposed to have occurred in the Late Cretaceous, based on adakitic granodiorite ages (>86 Ma, Zarrinkoub

et al., 2012), or mid-Eocene, based on tectono-stratigraphic interpretations (Tirrul et al., 1983). Felsic intrusions of the Bibi-Maryam pluton further to the south suggest slab melting in a pre-collisional intra-oceanic setting at 58.6 Ma (Delavari et al., 2014). In the South Sistan Basin, at a similar latitude as the Karvandar Basin, the timing of collision is controlled by syn-collisional erosion, the retreat of early- to mid-Eocene carbonate platforms (Mohammadi, Burg, et al., 2023), and sequences of mid-Eocene deep-water turbidites (McCall, 1997; McCall & Eftekhar Nezhad, 1994; Mohammadi, Burg, & Winkler, 2016). This age range is in agreement with felsic magmatic intrusions crosscutting the deformed accretionary prism (44–30 Ma), likely related to late- to post-collisional lithospheric delamination (Mohammadi, Burg, Bouilhol, & Ruh, 2016).

The SSZ consists of three major complexes that represent different tectono-stratigraphic sequences (Figure 1a): (a) In the east, the Ratuk Complex forms a pre-Maastrichtian accretionary wedge composed of imbricated metamorphosed sediments, lavas and highly deformed meta-ophiolites (Angiboust et al., 2013; Rad et al., 2005). (b) In the southwest, the Neh Accretionary Complex (NAC) represents the Paleocene/Eocene accretionary wedge stacking thick sequences of Late Cretaceous to Eocene deep-sea turbidites and slivers of Late Cretaceous ophiolites and Cretaceous platform carbonates (McCall, 1997; Mohammadi, Burg, & Winkler, 2016; Mohammadi, Burg, et al., 2023; Tirrul et al., 1983). The NAC also hosts several exotic assemblages such as the Karvandar Exotic Duplex and the Kuh-e-Birk consisting of ophiolites, platform limestones, marbles, schists, and volcanics (Bagheri & Damani Gol, 2020; Mohammadi, Burg, et al., 2023). (c) The Sefidabeh Complex unconformably overlays the NAC forming a wedge-top basin, consisting of clastic, volcanoclastic, and carbonate sediments (Tirrul et al., 1983). The frontal thrust of the NAC is often considered the western tectonic boundary of the SSZ, hence excluding the Karvandar Basin from being part of it (e.g., Bagheri & Damani Gol, 2020; Mohammadi, Burg, & Winkler, 2016; Figure 1a).

The SSZ is structurally overprinted by an active large-scale dextral strike-slip system that affects entire eastern Iran (e.g., M. Berberian et al., 1999, 2000; Freund, 1970; Walker & Jackson, 2004), induced by the indentation of the Arabian continent during the Zagros collision (Mattei et al., 2012), and accompanied by regional intra-plate alkali basaltic magmatism between 15 and 1.5 Ma (Pang et al., 2012; Walker et al., 2009). Furthermore, Jentzer et al. (2017) demonstrated how the principle stress orientation in the north Sistan rotated from purely compressional during the Miocene to dextral transpressional in the late Pliocene to present. Their temporal constraint contradicts with the Karvandar Basin being a strike-slip-related pull-apart basin already active in the Paleocene (Aghanabati et al., 1994; Bagheri & Damani Gol, 2020). Besides the tectonic overprint related to the SSZ and the East Iranian strike-slip system, the North Makran terranes south of the Karvandar Basin (Figure 1a) were imbricated and uplifted in the Miocene (~23–5 Ma) based on apatite fission track ages (Burg, 2018; Dolati, 2010), probably related to sediment underplating occurring across the Makran accretionary wedge (Platt et al., 1985). The uplift of the North Makran helped establishing the Jaz Murian as a forearc basin that, at least locally, was connected to the Karvandar Basin (Figure 1).

2.2. Karvandar Basin

The Karvandar Basin is an elongated structural basin west of the Karvandar Fault that has been proposed to represent the frontal fault, that is, western tectonic boundary, of the SSZ (Bagheri & Damani Gol, 2020). The local basin measures ~150 km in N-S direction and maximally 35 km along an E-W transect (Figure 1a) and was deposited onto the south-eastern margin of the microcontinental Lut Block (the easternmost microplate forming Central Iran). The Karvandar Basin consists of several doubly plunging synclines trending roughly N-S, parallel to the Karvandar Fault. The southern part of the basin consists of a single large syncline, while the basin becomes narrower toward the north, where several smaller dish-shaped synclines are closely assembled (Figure 1b). Anticlines are generally absent throughout the entire basin and synclines are separated by mud-dominated strata, which are in stratigraphic contact, or they are welded against each other (Figure 2). A prominent tuff horizon can be identified on satellite imagery in the northeastern syncline, which along its southern edge forms an angular unconformity, that is, a sedimentary onlap, potentially indicating syn-tectonic deposition (Figures 2c and 2d).

Detailed sedimentological mapping was not attempted previously (see area of geological mapping covered by Intercon-Texas Instruments in McCall (1997)). However, the detrital zircon U-Pb age population of a turbiditic sandstone sample in the southeast of the Karvandar Basin suggests an upper Eocene depositional age (Figure 1b; sample 134 from Mohammadi, Burg, and Winkler (2016)). These turbidites were potentially deposited into a shallow basin, demonstrated by the occurrence of patch reefs (Figure 1b). Strata overlaying Eocene deposits are composed of Oligocene to Pliocene shallow-marine and fluvial sediments, based on lower Miocene foraminiferal assemblages of one sample indicated on the Karvandar geological map of the Geological Survey of Iran

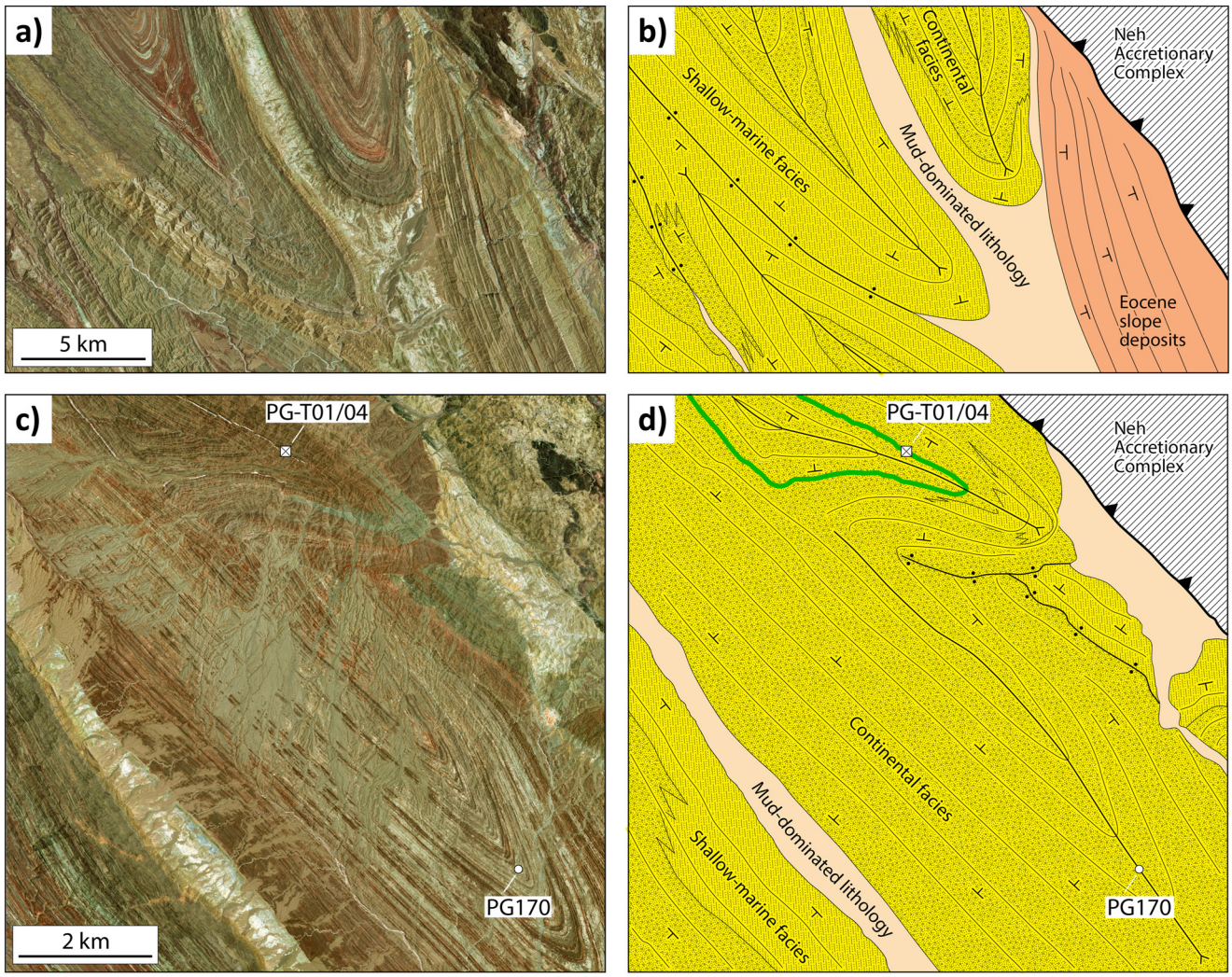

Figure 2. Satellite imageries (left) and corresponding interpretations of synclinal structures (right). Whitish colors in panels (a, c) indicate mud-dominated lithology underlying the shallow-marine to continental sequence. Imagery of the northern syncline (c) shows the ~25-m-thick tuff layer (samples PG-T01 and T04). Major angular unconformities, that is, onlaps, are visible. Locations outlined in Figure 1b.

(Figure 1b; Ghorashi & Vaezipour, 1987; McCall, 1997). However, data points are very scarce and the ages of the younger fluvial strata is interpretative. The exposure of Oligocene reefal limestones documented south of the Karvandar Basin (Huber, 1978) led McCall (1997) to argue that there has probably been a shallow sea extending westward toward Sirjan, where late Oligocene to Miocene reefal limestones are exposed (McCall et al., 1994). In this scenario, the Karvandar Basin is part of this shallow sea inland of the Mesozoic ophiolitic belt (Hunziker et al., 2015; Omrani et al., 2017; Saccani et al., 2018), which is currently mostly covered by Quaternary deposits in the Jaz Murian depression (McCall, 1997; Shahabpour, 2010).

At ~28°N latitude, mechanically weak Oligocene yellow-green shale with varying thickness crops out between the east- and west-dipping red sandstones and conglomerates of two synclines (Figure 1b). This narrow zone of shale hosts one of the largest mud volcanoes in Iran, the Pirgel mud volcano (Babadi et al., 2019; Negaresh, 2008; see Figure 3), indicating fluid overpressure at depth (e.g., Kopf, 2002). Mg-Li and Mg-K geothermometers of extruded muds indicated maximum temperatures of 107–153°C, implying a fluid source depth of ~3–7 km (Babadi et al., 2019).

3. Sedimentological Field Observations

According to Mohammadi et al. (2016b), the oldest sediments exposed in the Karvandar Basin (southeast) are middle to upper Eocene (youngest detrital zircon ages) marine slope deposits consisting of steeply WSW-dipping

10.1029/2023TC007971

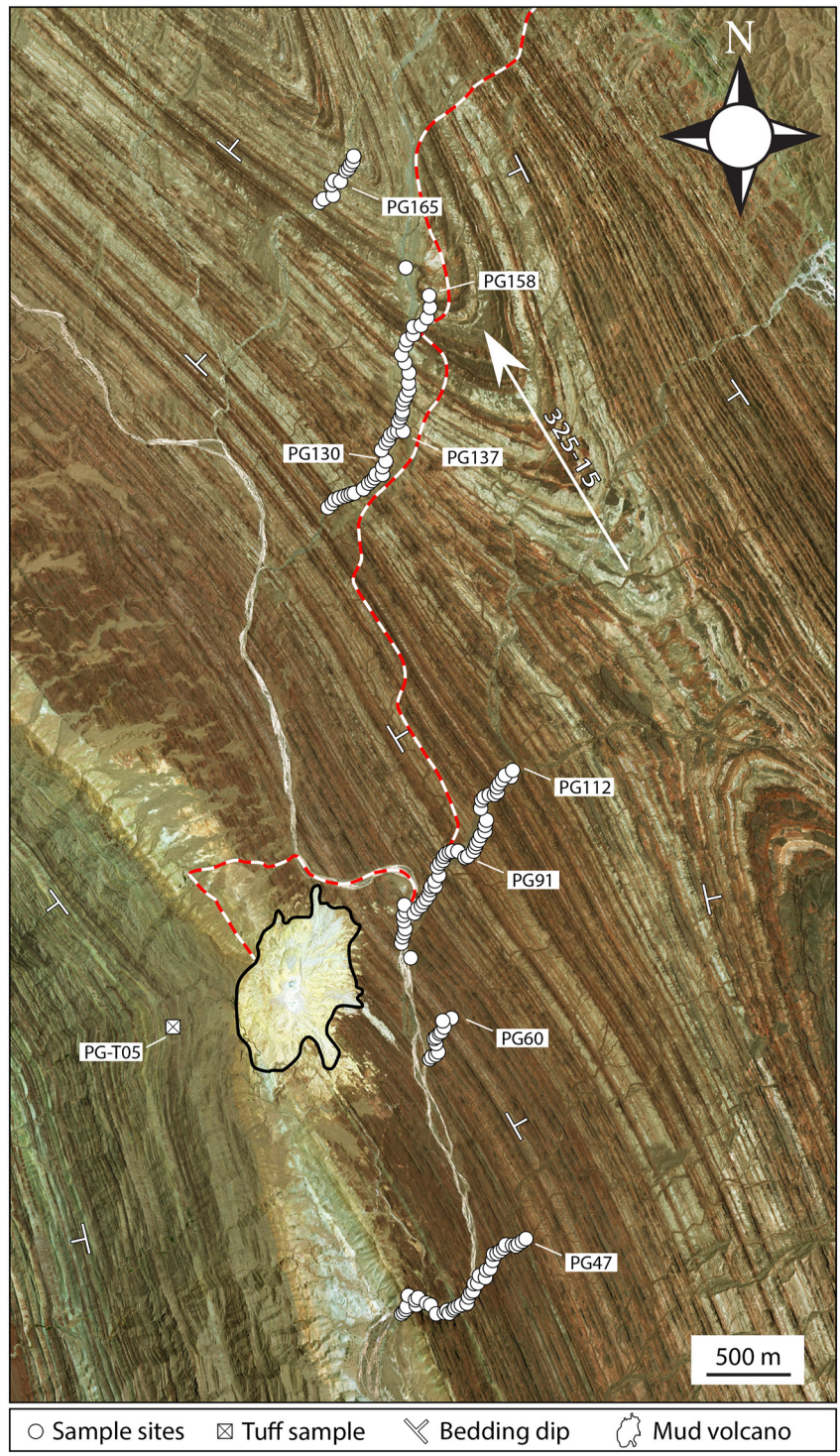

Figure 3. Sampling sites along the magnetostratigraphic section. Black line outlines the Pirgel mud volcano. Red-white dashed layer indicates the rural road leading to the mud volcano. Square shows the location of tuff sample PG-T05. PG170 indicates the position of the uppermost magnetostratigraphic section sample. White arrow indicates the orientation of the fold axis. Location outlined in Figure 1b.

marls and sandstones, with local occurrences of patch reefs pinching out within the arenaceous layers (Figure 1b). Above these layered Eocene deposits, a distinct 1–2-km-thick mud-dominated sequence is identifiable on satellite imagery due to its bright color (Figures 1b and 2). Our ~3,500-m-thick studied section begins with the first

10.1029/2023TC007971

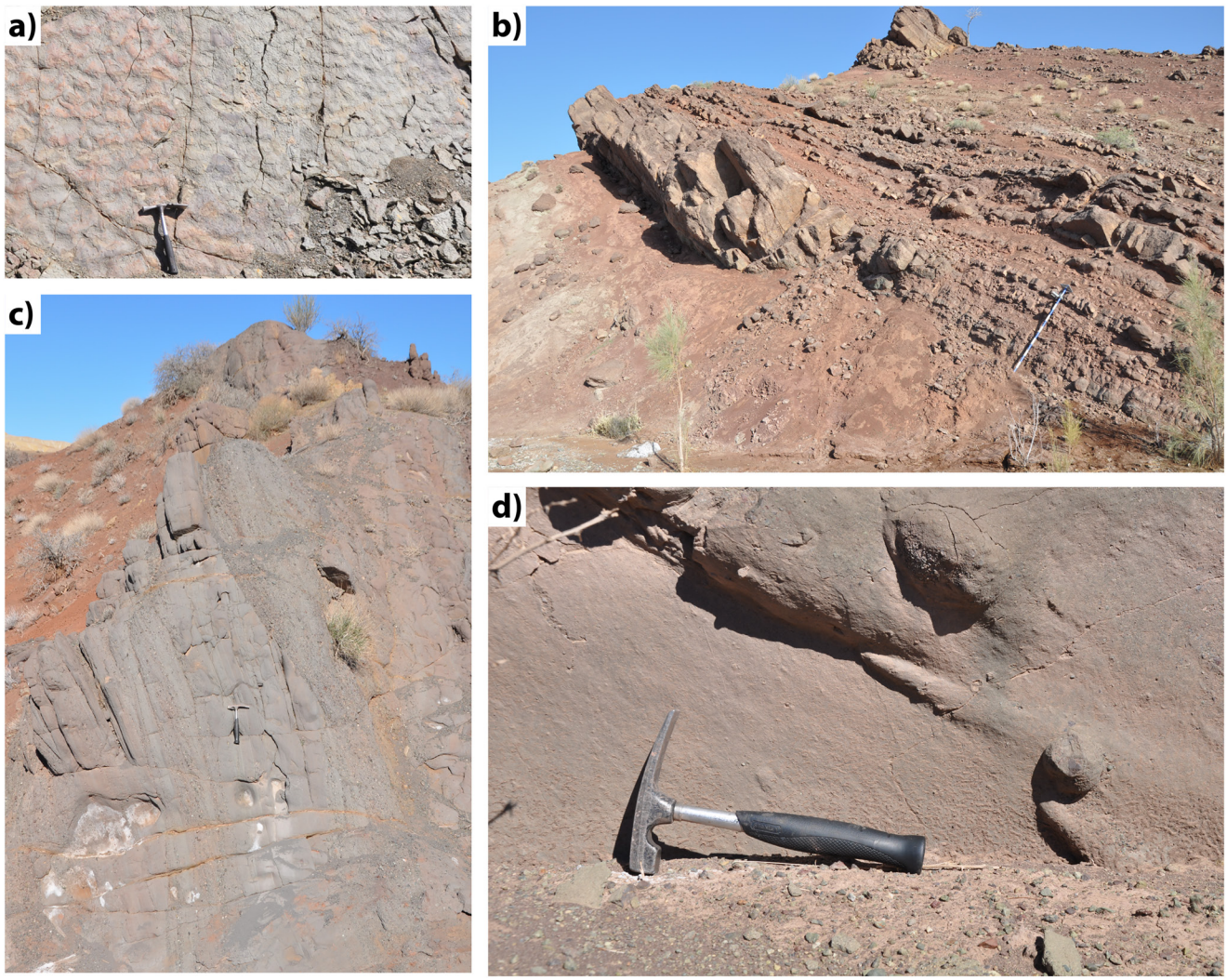

Figure 4. Photographs of lithologies in the studied section. (a) Thin-bedded sandstones with ripple marks of the shallow-marine lowermost part. (b) Vertically stacked conglomerate-sandstone intervals above finer-grained intervals. (c) Channelized coarse-grained sandstones and conglomerates. (d) Flute cast indicating flow direction.

occurrence of layered deposits covering the mud-dominated lithology (Figure 3). The base of this section correspond to a ~40-m-thick turbiditic interval dominated by mud, where fine-grained sandstones of centimetric and occasionally decimetric thickness with parallel lamination define the bedding. Above the turbidites, the occurrence of fine-grained sandstones with well-developed tractive depositional structures, such as ripple marks, and the scarcity of mud and silty beds indicate an increase in depositional energy (Figure 4a). The presence of carbonate beds rich in corals and large benthic foraminifera further supports this upward shallowing trend. This trend is also confirmed by the appearance of the first continental conglomeratic layer after 73 m into the section (Figure 5a). Above this stratigraphic level, an alternating sequence of conglomerate, sandstone, silt and clay dominates up to the top of the section. This depositional style is only interrupted by three marine incursions in the lowermost kilometer of the section, potentially linked to occurrences of sea level fluctuation or local short-lived basin subsidence (Figure 5a).

The conglomeratic unit within the Karvandar Basin exhibits distinct characteristics, consisting of amalgamated channels with sheet-like geometries (Figures 4b and 4c), often wider than several kilometers. Channels occur as multi-story fills with occasional trough and planar cross-stratification and tabular strata. Individual channel fills are generally 1–5-m-thick (Figures 6b and 6c), while vertically stacked amalgamated bodies reach up to 30 m in thickness, particularly above meter 3,300 in the section (Figure 5a). Fine-grained material, such as clays and silts, dominates some intervals (e.g., between meters 2,000–2,100 in the section). Sporadic carbonate-rich paleosoils

10.1029/2023TC007971

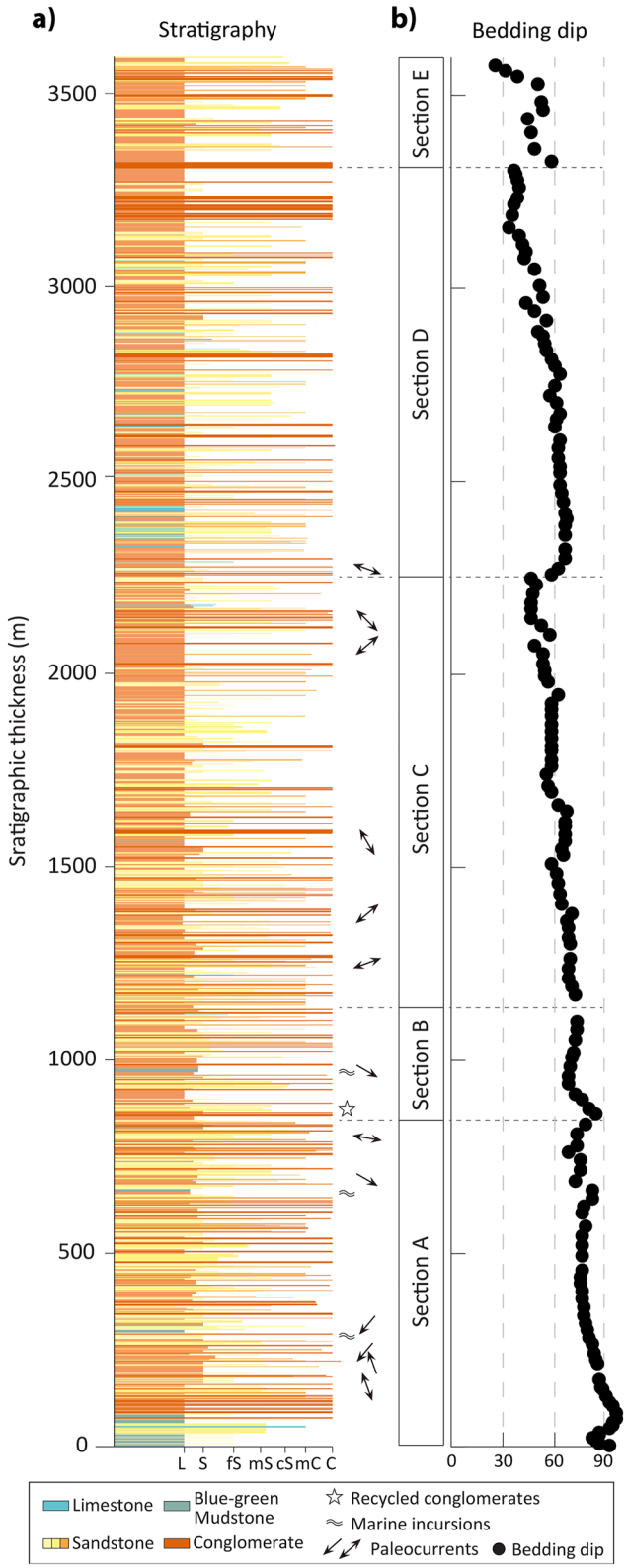

Figure 5. Stratigraphic section. (a) Detailed stratigraphic description with locations of selected paleocurrents, marine incursions, and first occurrences of conglomerate reworking. (b) Measured bedding dips.

develop among the fine-grained intervals, for instance at meters 1,560 and 2,400 (Figure 5a). The general architectural arrangement and facies association of the conglomerate unit suggest the depositional environment to represent the middle to distal parts of a distributive fluvial system with a distributed source area (Davidson et al., 2013; Huerta et al., 2011; Weissmann et al., 2010). The sequence was probably deposited with a high relative water discharge and high sediment supply (Hartley et al., 2010), likely under semiarid conditions (no organic beds, no plant remains, no lacustrine deposition). The general upward increase of conglomerate thickness and more frequent occurrences of paleosoils suggest retrogradation, basin fill-up, and a farther shoreline upwards over time. The high sediment supply compensates for the high subsidence rate, resulting in a long-term trend of sediment accumulation and filling of the basin.

Sedimentary bedding is steep and partly overturned in the lowermost 100 m of the sampled section (Figure 5b). Across the magnetostratigraphic section, the bedding of the clastic strata flattens continuously within each subsection to reach dip values of ∼30° at the top.

The Pirgel mud volcano is located at coordinates 27°59′20″N and 60°29′03″E and is squeezed in between the two nearly welded northern synclines (Figure 3). The mud volcano and its extrusion product cover an area of ∼1 km^2 with a vertical relief of ∼100 m relative to the surrounding areas (Figure 6a). The mud volcano consists of a central plateau (Figure 6a) with several active and inactive mud gryphons and pools (Figure 6b).

The poorly lithified mudstones forming the frame of the mud volcano contain centimeter- to meter-scaled randomly oriented angular to sub-rounded blocks of mostly volcanic (andesitic) material (Figure 6c). In addition to the volcanic blocks, there are also fewer occurrences of corals within the mudstones (Figure 6d). Pebbles of the same composition as the larger blocks furthermore cover the mud edifice surface (Figures 6c and 6d), except in places where fresh mud flows appear (Figure 6b). It is noteworthy that these pebbles and blocks are not found anywhere else throughout the investigated area, suggesting a localized source or transport mechanism specific to the mud-dominated lithology.

4. Methodology

4.1. Magnetostratigraphic Sampling and Measurements

Due to the limited transport infrastructure, magnetostratigraphic sampling was conducted on the north-eastern syncline of the Karvandar Basin. This section was accessible via a dirt road that connects the Pirgel mud volcano with the Zahedan-Iranshahr main road to the east of the basin (Figure 3). To cover the entire section comprehensively, we divided it into five subsections, following dry river creeks crosscutting the sedimentary sequence. A total of 170 sites were sampled, starting from the south of the Pirgel mud volcano (Figure 3). At each site, cores of mud-, silt- or fine-grained sandstone were sampled with a battery-driven drill. The spacing between sampling sites range between 10 and 25 m depending on the suitability of lithologies for magnetostratigraphy, considering a high sedimentation rate setting, similar to other conglomerate-dominated foreland basins, where accumulation rates of >100 cm/kyr were observed (e.g., Schlunegger et al., 1997).

Natural remanent magnetization (NRM) of the samples were measured during stepwise thermal demagnetization using a tri-axial DC superconducting quantum interference device rock magnetometer (2G Enterprise 755R) with a sensitivity of ∼3·10^{-8} A/m at the Laboratory for Natural Magnetism at ETH Zurich. The NRM and thermal demagnetization process included 20 steps

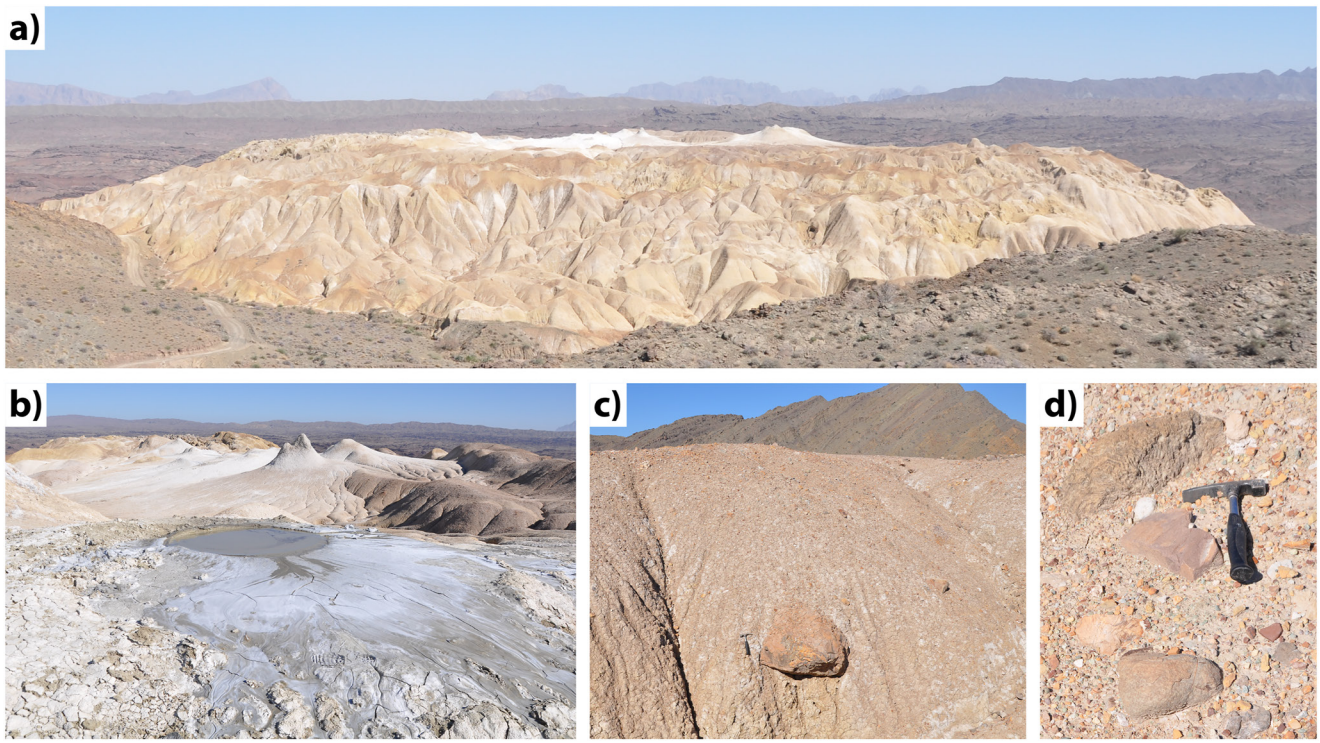

Figure 6. Photographs of the Pirgel mud volcano and the mud-dominated lithology. (a) Eastward view of the mud volcano. (b) Active mud gryphon in front, inactive mud cone in back. (c) Sub-angular volcanic block in mud matrix. (d) Volcanic and coral pebbles covering the mud volcano.

from 0°C to 680°C, with intervals of 50°C up to 400°C, 20–30°C up to 660°C, and 10°C up to 680°C. Sample heating was conducted with an ASC TD48 oven (internal field <5 nT). The resulting demagnetization paths were plotted on vector diagrams for the identification of different magnetic components, unblocking at different temperatures (Zijderveld, 1967). The program Remasoft was applied to identify distinct magnetic components (Chadima, 2006), where line fitting of principal components was achieved by the method of Kirschvink (1980) and statistical parameters of magnetic directions were calculated by the method of Fisher (1953). Magnetic susceptibility of all samples was measured before each heating step with an AGICO KLY 2 Kappabridge in order to monitor mineralogy changes related to the heating. Remasoft-type files (.rs3) of each measured sample are found in Data Set S1.

4.2. Framework Composition and Paleocurrents

Along the same section, a sandstone and microconglomerate framework study was performed aiming to identify detrital grain types and interpret their source areas. Modal framework analysis was carried out on 55 medium- to coarse-grained sandstones. For each sample thin-section, at least 300 points were counted following the Gazzi-Dickinson point-counting method (Ingersoll et al., 1984). Additionally, 14 microconglomerate samples were analyzed, where at least 100 granule grain points were counted per sample thin-section. Attention focused on identifying rock fragments to define the fabric, texture, and lithology of the parent rocks. Results are presented in standard complementary ternary diagrams (Dickinson, 1985; Dickinson & Suczek, 1979; Folk, 1980).

A total of 32 paleocurrent indicators were measured across the sampled section, including grooves, flute casts, tool casts/marks, erosion channels and cross-bedding. Paleocurrents were separated into 11 directional and 21 non-directional orientations depending on whether a clear transport direction could be interpreted. Measurements were rotated to a horizontal plane around the strike direction of bedding.

4.3. Zircon U-Pb Geochronology

Two prominent tuff layers were detected in the Karvandar Basin and sampled for zircon dating to provide independent age constraints for the magnetostratigraphy. A ~50-cm-thick tuff layer was sampled at the base of the

northwestern syncline, ~500 m west of the Pirgel mud volcano (Figure 3). Considering the dip of the marine strata of 45° at the base of the western syncline results in stratigraphic position of ~350 m in section. As both the bases of the western and eastern syncline are in direct stratigraphic contact with the underlaying mud-dominated lithology, the tuff layer is expected to be positioned at the same stratigraphic level in the eastern syncline, where the magnetostratigraphic section was sampled. There however, first arrivals of conglomerate probably eliminated the thin tuff horizon. In addition, two samples were collected from a ~25-m-thick tuff horizon situated several kilometers to the north of the magnetostratigraphic section, as indicated on the Ziruki-ye-Goharkuh geological map of the Geological Survey of Iran (Figure 2c; Z. Hosseini & Afsharianzadeh, 1993).

The U-Pb ages of individual zircon grains of the tuff layers were analyzed using laser ablation inductively coupled mass spectrometry (LA-ICP-MS) at the Institute of Geochemistry and Petrology at ETH Zurich with a similar analytical protocol as applied in Guillong et al. (2014). The measurements were conducted with a laser repetition rate of 4 Hz, an energy density of ca. 2 J/cm^2 and a spot diameter of 19 µm. The raw data was corrected by primary reference material "GJ-1" (601.86 ± 0.37 Ma, Horstwood et al., 2016), and the secondary RMs "Plešovice" (337.13 ± 0.37 Ma, Sláma et al., 2008), "91500" (1,063.51 ± 0.39 Ma, Wiedenbeck et al., 1995), "AusZ7-1" (38.896 ± 0.01 Ma, Kennedy et al., 2014), and "AusZ7-5" (2.41 ± 0.01 Ma, von Quadt et al., 2016) were analyzed for quality control. The measured data was plotted on Concordia diagrams using the IsoplotR software (Ludwig, 2003; Vermeesch, 2018). Uncertainties are given as 2SE and "SE including 1.5% systematic external uncertainty (Horstwood et al., 2016). Only concordant measurements of $^{206}Pb/^{238}U$ and $^{207}Pb/^{235}U$ ages were considered for all three samples to ensure the exclusion of data affected by lead loss and initial Pb. Both cores and rims of zircon single grains were targeted to detect and exclude inherited crystallization ages (Figure S1 in Supporting Information S1).

4.4. Calcite U-Pb Geochronology

Calcite U–Pb dating was performed on a coral sample collected from the Pirgel mud volcano (Figure 3). The polished sample was examined using LA-ICP-MS by the same instrument as for zircon dating (see Section 4.3.), but with a laser repetition rate of 5 Hz and a spot diameter of 110 µm. Variable single-spot ablation signals were integrated independently following the method described by Guillong et al. (2020). The raw data was corrected by primary RMs "NIST 614" and "WC-1" (254.4 ± 4 Ma, Roberts et al., 2017) and secondary RMs "JT" (13.797 ± 0.031 Ma, Guillong et al., 2020) and "ASH-15D" (2.965 ± 0.011, Nuriel et al., 2021) were analyzed for quality control. U–Pb ages were interpreted from the lower intercepts of Tera-Wasserburg Concordia diagrams using the IsoplotR software (Ludwig, 2003; Vermeesch, 2018). Uncertainty is given as 2SE and "SE including 2.5% systematic external uncertainty (Guillong et al., 2020).

4.5. Nannofossils and Foraminifera

Three liquid samples collected from active mud pools and gryphons of the Pirgel mud volcano were analyzed to identify their micropaleontological content (calcareous nannofossils and foraminifera) to obtain a first-order age control of the source lithology. For the nannofossil content, the samples were prepared according to the smearing technique in order to prevent assemblage selection and to retain the original composition (Bown & Young, 1998). The analyses were performed using a polarized light microscope with a magnification of 1250X. Nannofossil assemblages were semi-quantitatively estimated by counting all the nannoliths recorded in 300 fields of view. Taxonomic attribution follows Perch-Nielsen (1985), Bown and Young (1998), and the website https://mikrotax.org/Nannotax3 (Young et al., 2017). Calcareous nannofossil content was described with reference to Agnini et al. (2014) and Backman et al. (2012).

For the analysis of foraminiferal content, the same samples were prepared as washed residues following standard procedures. The muddy mixture was washed and sieved (with mesh sizes of 425, 150, and 63 µm). The obtained washed residues were then oven-dried for one day at 40°C and examined under a stereomicroscope at magnifications varying from 6.3 to 50X. Taxonomic attribution of planktonic marker species are based on the online catalog "pforam@mikrotax" (http://www.mikrotax.org), integrated by the online World Foraminifera Database (http://www.marinespecies.org/foraminifera; Hayward et al., 2022) for benthic taxa.

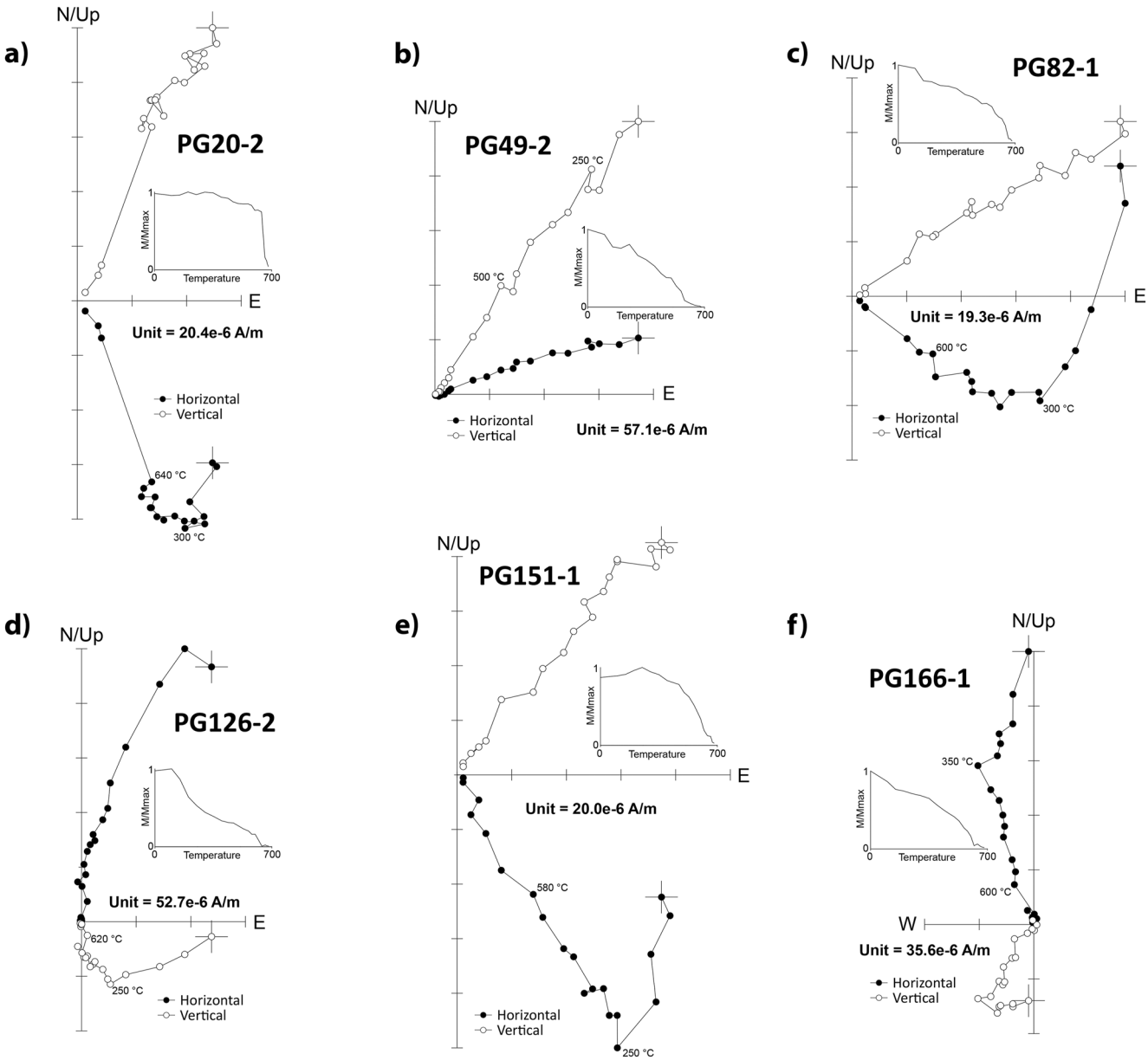

Figure 7. Selected diagrams of tilt-corrected Natural remanent magnetization thermal demagnetization curves. White and black dots represent vertical and horizontal projections (after Zijderveld (1967)) of (d, f) normal and (a–c, e) reversed polarities.

5. Results

5.1. Magnetostratigraphic Analysis

The NRM of all measured samples display values larger than $3{\cdot}10^{-6}$ A/m with a mean value of $1.1{\cdot}10^{-4}$ A/m, slightly increasing toward the top of the section (Figure S2 in Supporting Information S1). A similar tendency can be observed for the dimensionless magnetic susceptibility χ (SI), which displays values of 10^{-4}–10^{-3} in the lower part and 10^{-3}–10^{-2} in the upper part of the section (Figure S2 in Supporting Information S1). This increase indicates an increasing magnetite concentration toward the top of the section. The resulting normalized intensity (NRM/χ) shows no significant variation across the entire section ($\sim 10^{-1}$ A/m; Figure S2 in Supporting Information S1). Representative thermal demagnetization curves reveal that most samples (89%) contain a low-temperature magnetic component that is removed at temperatures of 250–300°C (Figure 7). An additional stable magnetic component is found in 96% of the measured samples, typically fully demagnetized above 620°C,

10.1029/2023TC007971

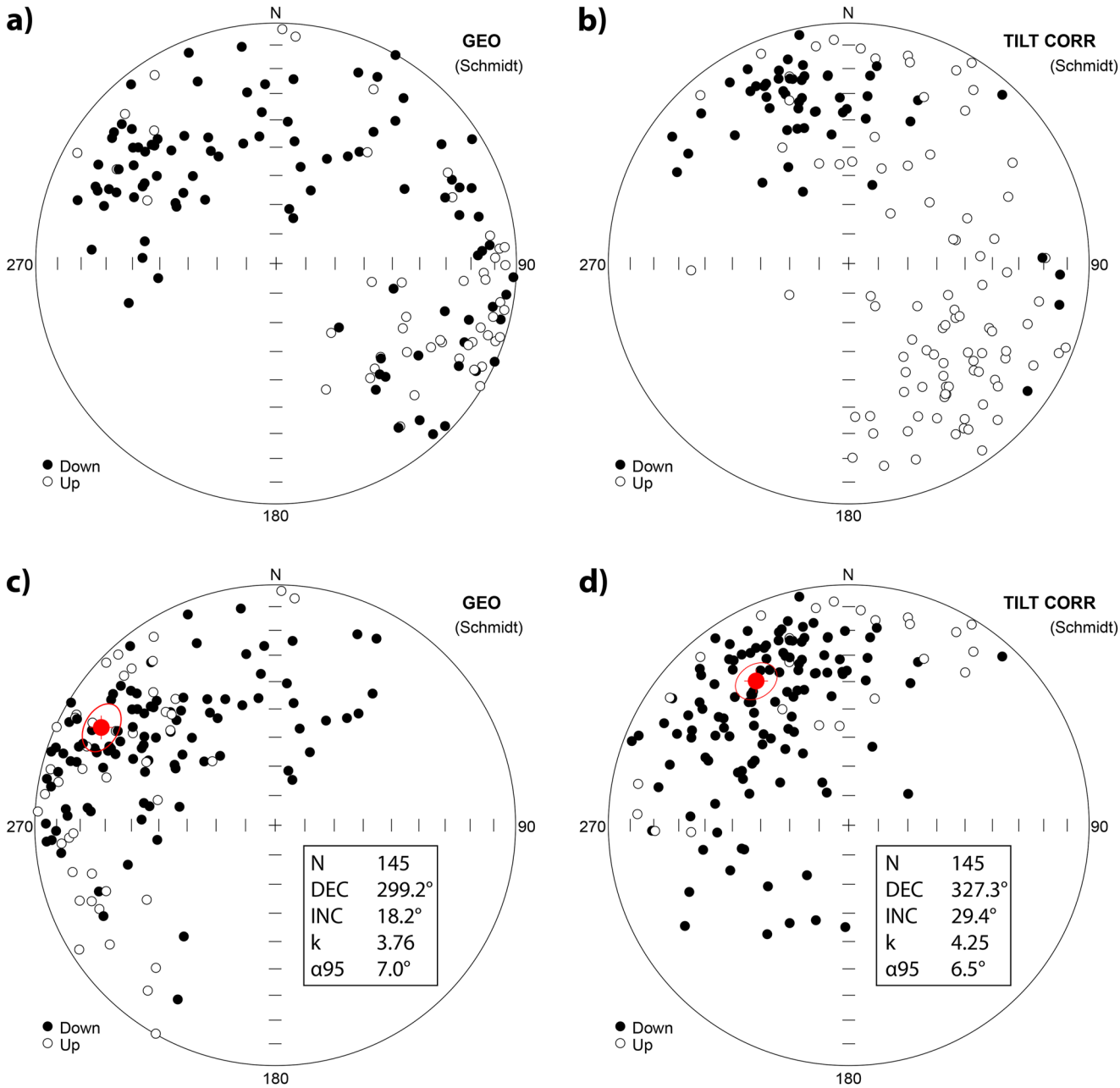

Figure 8. Paleomagnetic characteristic remanent magnetization (ChRM) directions, without and with tectonic tilt-correction. (a, b) All samples with clear ChRM. (c, d) All ChRM transposed onto same hemisphere for statistical significance. Mean direction of tilt-corrected transposed data indicate a counter-clockwise rotation of ~30° (d).

indicating hematite as the primary magnetic carrier (Figure 7). Characteristic remanent magnetic components (ChRM) are classified depending on the median absolute deviation of the demagnetization curve, where type 1 indicates a MAD ≤ 10 (44%), type 2 a MAD ≤ 20 (45%), and type 3 a MAD > 20 (11%). Only samples with quality type 1 and 2 are used to constrain the magnetopolarity stratigraphy (MPS). All paleomagnetic data can be found in Table S1.

Statistical grouping of the low-temperature magnetic components (without correcting for bedding tilt) yields a mean direction with a declination of 3° and an inclination of 42.3°, with a strong statistical significance (Figure S3 in Supporting Information S1), and is similar to the present Earth's magnetic field direction at the corresponding longitude and latitude (dec: 1.5° and inc: 43.1°).

Of the 170 measured samples, 145 manifest ChRM directions of quality type 1 and 2 (MAD ≤ 20). These magnetic directions are projected onto lower-hemisphere equal-area Schmidt nets before (Figure 8a) and after correcting for bedding tilt (Figure 8b). Tilt-corrected magnetic directions indicate both normal and reversed polarities, showing an antiparallel distribution (Figures 8a and 8b). To obtain the mean orientations for all 145 samples before and after tilt correction, ChRM directions are transposed onto the same hemisphere (Figures 8c and 8d). The statistical distribution of tilt-corrected directions is slightly more significant ($k = 4.25$, $\alpha_{95} = 6.5°$) than uncorrected direction ($k = 3.76$, $\alpha_{95} = 7.0°$), although only to an irrelevant degree. The resulting mean of the transposed tilt-corrected magnetic directions shows a declination of 327.3° and an inclination of 29.4° (Figure 8d).

The tilt-corrected ChRM directions were used to calculate the virtual geomagnetic pole (VGP) for each individual sample, considering the sampled site location using a longitude of 60.5°E and a latitude of 28°N (Figure 9). For samples PG130–170, a fold axis with an orientation of 325-15 was additionally applied for tilt correction, related to the syncline geometry to the north (Figure 3). Corrected VGP directions are calculated for tilt-corrected ChRM directions rotated 30° in clockwise orientation, corrected for the apparent rotation shown by the tilt-corrected ChRM directions (Figure 9e). The resulting VGP_{corr} is used to define the magnetic polarity of each ChRM, where positive VGP_{corr} latitudes represent normal polarities and negative VGP_{corr} latitudes reverse polarities. Sixty samples exhibit VGP_{corr} latitudes of ≥45° and are considered clearly positive, while 61 samples exhibit latitudes of <−45° that are considered clearly reverse. Forty-two samples exhibit VGP_{corr} latitudes between −45° and 45° and are considered transitional, either indicating polarity switches, polarity excursions, or a ChRM affected by a secondary magnetization. To construct the local MPS, at least two consecutive samples of quality type 1or 2 with a clear polarity ($VGP_{corr} \geq |45|$) are required. This results in a robust reversal patter for sections B to E, and a less robust pattern for section A, with several occasions of single reverse ChRM's (Figures 9e and 9f).

A reversal test was conducted to verify the antiparallel configuration of the normal and reverse magnetic directions (McFadden & McElhinny, 1990). A reversal test is considered successful if the transposed mean direction of one polarity group lays within the 95% confidence level (α_{95}) of the other polarity group. The paleomagnetic data set of this study does not pass the reversal test. This can be due to the relatively high percentage of transitional ChRM directions that mostly plot in the northeastern quartile of the lower hemisphere Schmidt net (Figure 8b) and therefore close the angle between the two mean directions. Another reason may be a secondary NRM that could not have been fully removed from individual ChRM's. However, the importance of the reversal test diminishes when it comes to magnetostratigraphy, as magnetic polarity can frequently be determined from partially overlapping paleomagnetic orientations (Garcés, 2015).

Furthermore, fold tests were conducted independently for both normal and reverse polarity groups (Tauxe & Watson, 1994), regarding the variable bedding dip across the magnetostratigraphic section (Figure 5b). Fold test of both polarity clusters show a more significant statistical grouping for unfolded strata (Figure S4 in Supporting Information S1).

5.2. Framework Composition and Paleocurrents

Across the investigated section, sandstones are predominantly medium- to very-coarse-grained, moderately sorted, with sub-rounded to angular grains (Figure S5a in Supporting Information S1). These sandstones are rich in first-cycle rock fragments, corresponding to litharenite/volcanic arenites (Figure 10a). Among the rock fragments, volcanic lithic fragments are the most abundant accounting for an average of 77% of the total lithic grains (Table S2). Microlithic andesites, basalts and diabase are the main components of the volcanic lithic fragments (Figures S5b–S5d in Supporting Information S1). Metamorphic lithic fragments make up about 15% of total lithic grains and are mainly composed of slate, quartz-sericite, chloritoschist and prasinite lithic fragments (Figures S5e–S5h in Supporting Information S1). Other components present in smaller proportions include radiolarian cherts (4%), siltstones (2%), ultramafic grains (2%) and extra-basinal carbonates (Figures S6a–S6d in Supporting Information S1). On average, 22% of all grains are quartz, of which ∼75% are monocrystalline (Table S2). Monocrystalline quartz grains exhibit idiomorphic volcanic shapes with straight sides and rounded corners (Figure S6e in Supporting Information S1). Polycrystalline quartz grains, on the other hand, are predominantly recrystallized, schistose and stretched metamorphic types with multiple sub-grains (Figures S6f–S6g in Supporting Information S1). Feldspars make up about 11% of the modal composition (Figure S6h in Supporting Information S1), with ∼67% of them being plagioclase. Standard provenance ternary diagrams

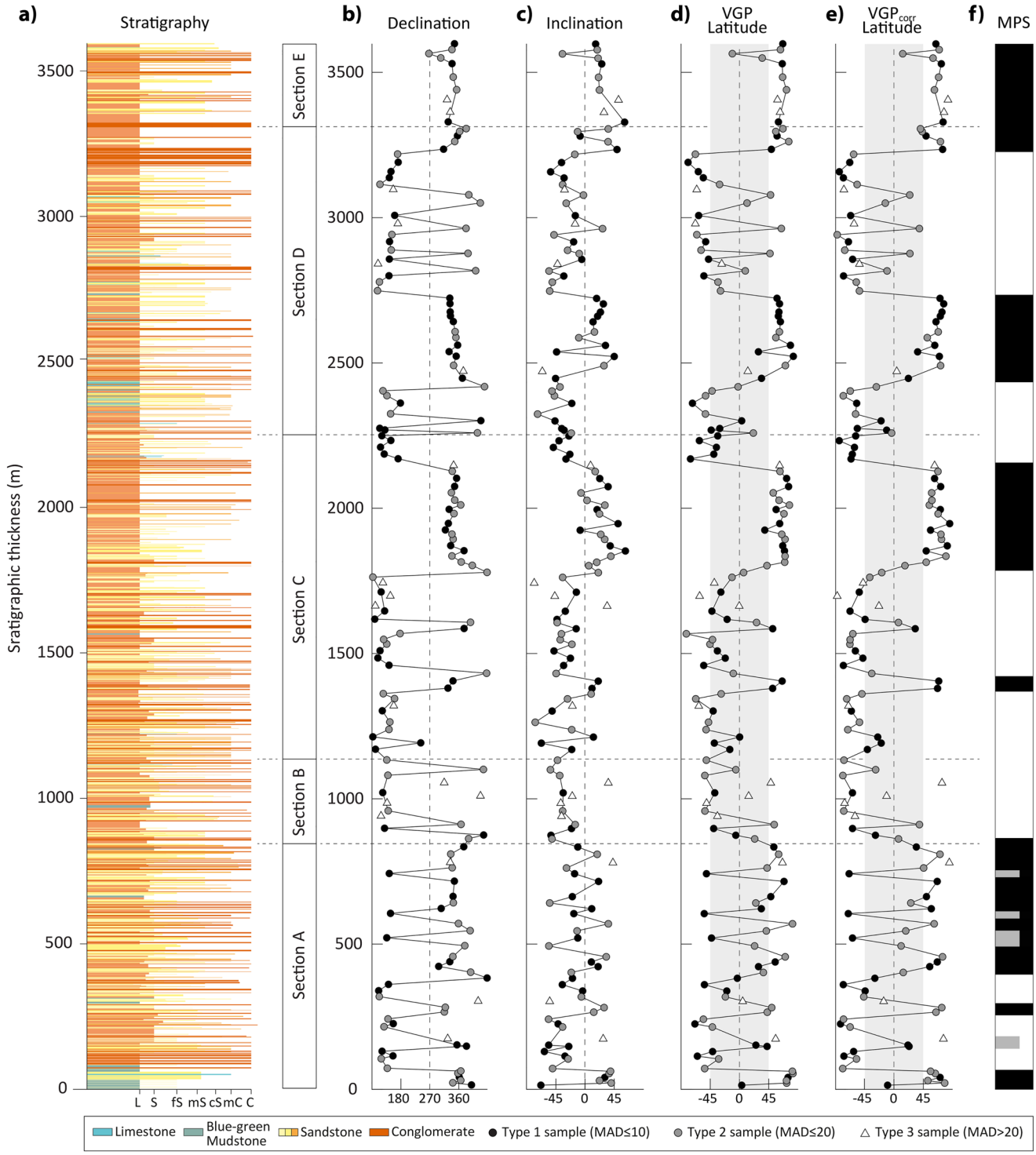

Figure 9. Magnetostratigraphic section. (a) Detailed stratigraphic log. (b) Declination of ChRM. (c) Inclination of ChRM. (d) Virtual geomagnetic pole latitude (VGP). (e) VGP corrected for a 30° counter-clockwise rotation (VGP$_{corr}$). (f) Local magnetopolarity stratigraphy inferred from VGP$_{corr}$.

(Dickinson, 1985) display average grain compositions of $Qt_{25}F_{11}L_{64}$ and $Qm_{16}F_{11}Lt_{73}$ and Karvandar sandstones mainly plot in the fields for transitional to undissected arcs and/or recycled orogens (Figures 10b and 10c).

Granules in sampled polymictic microconglomerates are dominated by rock fragments (93%, Table S3). Angular andesitic-basaltic volcanic rock fragments are the most abundant grains (71%, Figures S7a and S7b in Supporting

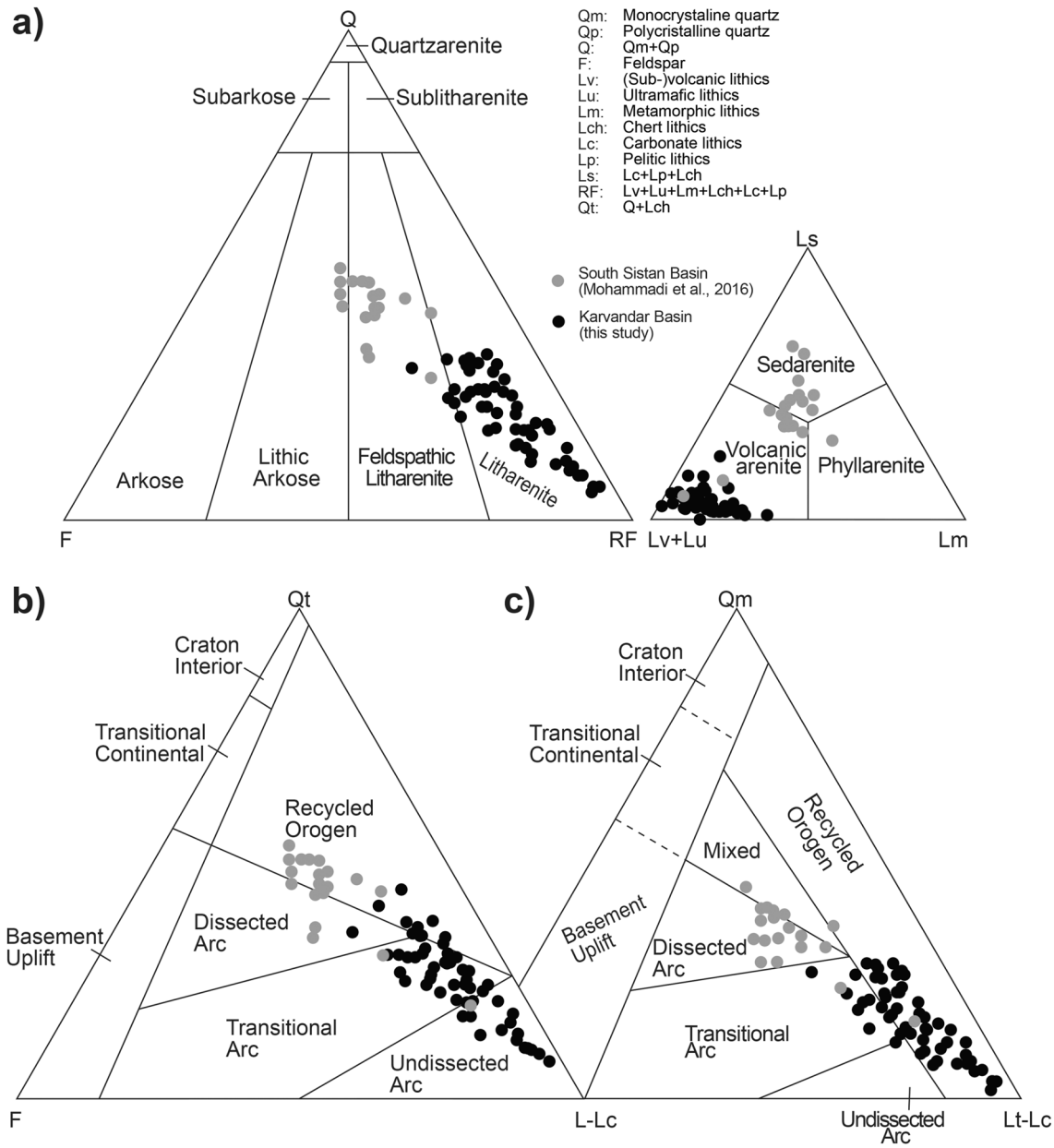

Figure 10. Detrital composition and classification on triangular (a) QFRF (Folk, 1980), (b) QtFL, and (c) QmFLt (Dickinson, 1985). Detailed data and definitions are given in Tables S1 and S2. Black dots: Karvandar sandstones. Gray dots: Sandstones from the South Sistan Basin (Mohammadi, Burg, & Winkler, 2016).

Information S1). Metamorphic lithics are represented by slate, prasinite and amphibolite, and constitute on average 21% of the lithic grains (Figures S6c–S6e in Supporting Information S1). In addition, minor components including radiolarian cherts (5%), siliciclastics (2%), and ultramafic grains (1%) were detected (Figure S7f in Supporting Information S1). The crystal content of the microconglomerates is on average 7% of the modal composition and mostly consists of polycrystalline metamorphic quartz grains (Figures S7g and S7h in Supporting Information S1).

The stratigraphic trend along the sampled section in terms of sandstone classification remains relatively consistent, with no major deviation from the overall average composition with 22% quartz, 11% feldspar, and 67% rock fragments (Figure 11c). However, a notable increase in metamorphic lithic grains can be observed toward the top of the section, potentially causing the increase in magnetite content manifested by magnetic susceptibility (Figure S2 in Supporting Information S1). Furthermore, rock fragments of sandstones show a slightly higher

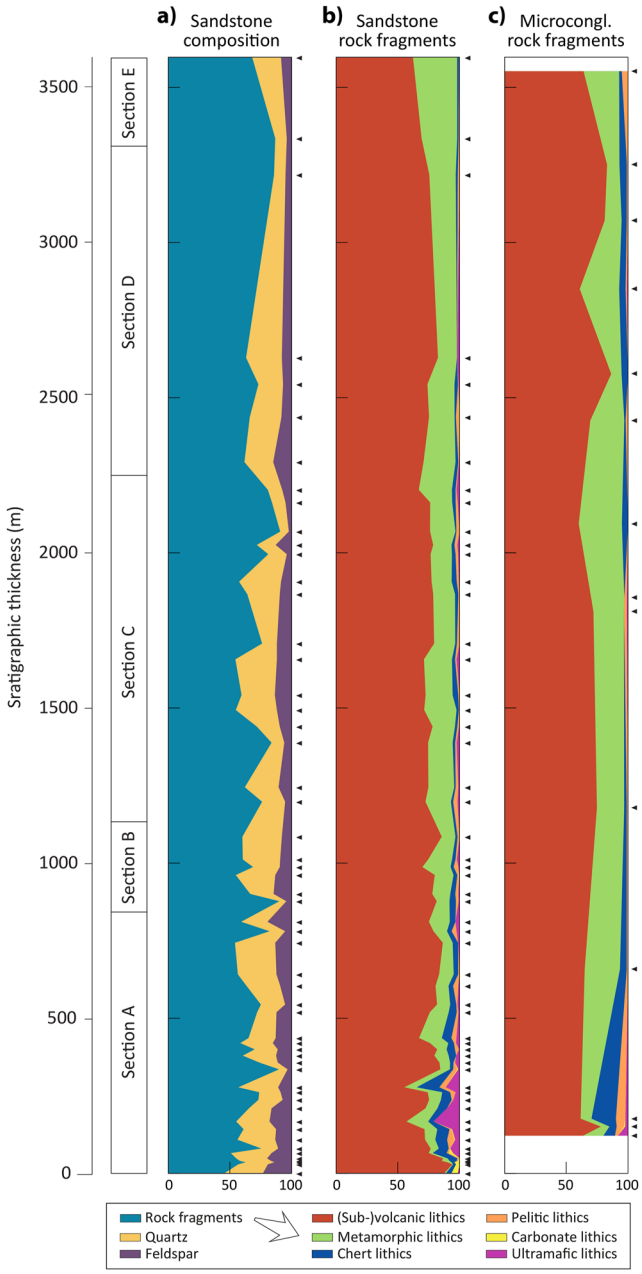

Figure 11. Sediment framework along the sampled section. (a) Variation in sandstone framework. (b) Variations in sandstone rock fragment composition. (c) Variations in microconglomerate fragment composition.

abundance of ultramafic, chert, siliciclastic, and carbonate grains at the base of the section (Figure 11d). Microconglomerates exhibit a similar pattern, with slightly higher abundances of chert, pelitic, and ultramafic grains at the base (Figure 11e).

The paleocurrents measured on flute casts with a clear flow direction (Figure 4d) indicate a general northeast to southwest transport direction (Figure 12a). Paleocurrent measurements based on bi-directional symmetric ripple marks and tool marks show similar orientations with a dominant northeast-southwest component (Figure 12b). The obtained orientations are similar to paleocurrent directions from the neighboring Eocene Neh Complex (Figure 12c, Mohammadi, Burg, & Winkler, 2016).

5.3. Zircon U-Pb Ages

Samples PG-T01 and T04 represent the base and the top of a ~25-m-thick andesitic tuff horizon in a concentric syncline located several kilometers north of the magnetostratigraphic section deposited after the last collected sample site PG170 (Figures 2c and 2d). Zircon grains show oscillatory zoning indicative of magmatic growth and sometimes contain cores that are 1–5 Myr older (Figures S1a and S1b in Supporting Information S1). Some zircons exhibit Ediacaran cores (Figure S1b in Supporting Information S1). Concordant crystallization ages of 11 single grain zircons of the andesitic tuff sample PG-T01 result in a Concordia age of 17.65 ± 0.14 | 0.30 Ma (Figure 13a). The Concordia age of sample PG-T04 is 17.81 ± 0.13 | 0.30 Ma based on 11 single grain zircon ages (Figure 13b). Zircons of tuff sample PG-T05 from the base of the shallow marine succession west of the Pirgel mud volcano (Figure 3) also show two phases of growth with round to angular cores and oscillatory overgrowth (Figure S1c in Supporting Information S1). The youngest concordant cluster of 24 U-Pb zircon ages indicates a crystallization age of 22.84 ± 0.16 | 0.38 Ma (Figure 13c). Isotopic ratios and ages are given in Table S4.

5.4. Calcite U-Pb Ages

Figure 14a shows an image of the thin section of coral sample PG-Pir05 under cross-polarized light. The sample was collected from a larger block found within the mud matrix on the Pirgel mud volcano (Figure 3). A total of 58 calcite U-Pb age point measurements yield a discordant lower intercept age of 24.49 ± 1.15 | 1.30 Ma (Figure 14b). A mean square weighted deviation of 0.44 indicates a closed system behavior (Guillong et al., 2020). Isotopic ratios are given in Table S5.

5.5. Nanno- and Foraminiferal Age Constraints

Nannofossil assemblages from extruded mud include *Cyclicargolithus abisetctus*, *Cyclicargolithus floridanus*, *Discoaster deflandrei*, *Sphenolithus dissimilis*, and *Sphenolithus moriformis* (Table S6). Although zonal markers were not recorded, maybe because in very poor materials only heavily calcified species of assemblages are preserved, samples can be referred tentatively to the Oligocene-Miocene transition interval.

Foraminiferal assemblages were abundant and characterized by both planktonic and benthic specimens. The most common species are upper Oligocene-lower Miocene taxa, such as the planktonic *Ciperoella cipereonsis*, *Ciperoella angulisuturalis*, *Dentoglobigerina venezuelana*, *Globigerinoides primordius*, *Paragloborotalia nana*

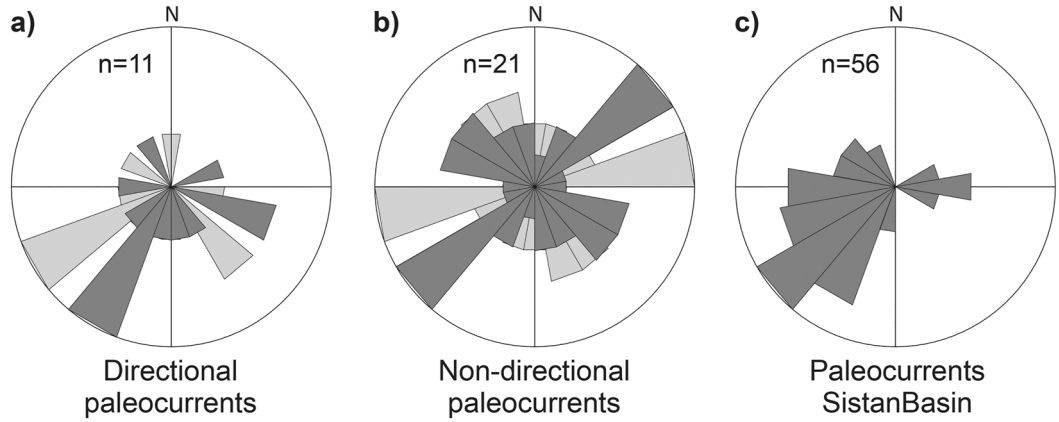

Figure 12. Rose diagram indicating (a) directional and (b) non-directional paleocurrent orientations from the Karvandar Basin with dominant southwest directions. (c) Paleocurrents from the South Sistan Basin for comparison (Mohammadi, Burg, & Winkler, 2016). Light gray in panels (a, b) indicate paleocurrents from the Karvandar Basin corrected for an observed counter clock-wise rotation of 30°.

and the benthic *Protoglobobulimina pupoides*, *Cibicidoides ungerianus*, *Arenobulimina* sp., and *Anomalinoides* spp (Table S7). In sample PG-M01, one single Cretaceous specimen of *Marginotruncana* sp., particularly well preserved, was recorded.

6. Discussion

6.1. Age Constraints on the Deposition of the Karvandar Basin

To establish the temporal framework for the deposition of the Karvandar Basin, the results of different dating techniques were combined. The U-Pb zircon ages of three tuff layers (Figure 13) and the U-Pb calcite age of the coral block within mud deposits of the Pirgel mud volcano (Figure 14) help correlating the MPS with the geomagnetic polarity time scale (GPTS, Gradstein & Ogg, 2020). The U-Pb calcite dating of the coral sample taken from a block within the mud-dominated lithology provides an age of 24.49 ± 1.15 | 1.30 Ma (Figure 14b), indicating a maximum age for the base of the neritic-continental sequence that overlies the mud-dominated lithology. Furthermore, nannofossil and foraminiferal assemblages from extruding mud samples of the Pirgel mud volcano suggest a Chattian-Aquitanian depositional age (Tables S6 and S7). The age constraint provided by tuff sample PG-T05 (Figure 13c, 22.84 ± 0.16 | 0.38 Ma) at ~350 m from the base of the western syncline (Figure 3) offers a minimum age estimate for the base of the shallow marine to continental sequence. Furthermore, it position in the magnetostratigraphic section of the eastern syncline is estimated to ~300–450 m from the base, based on similar to slightly increased sediment accumulation rates of the first conglomerate layers. The

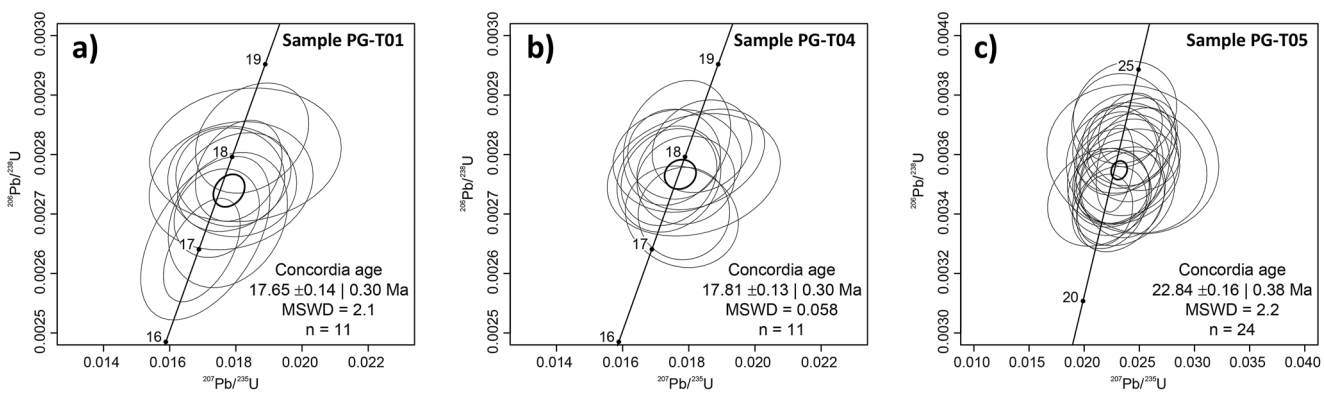

Figure 13. U-Pb zircon ages of three tuff samples. (a, b) Sample PG-T01 and T04 are from northern syncline (location in Figures 2c and 2d) at the top of the section. (c) Sample PG-T05 is from western syncline (location in Figure 3) at the bottom of the magnetostratigraphic section. Only concordant ages were used to constrain final age. Uncertainty ellipses are 2SE. See Table S4 for isotopic ratios and ages.

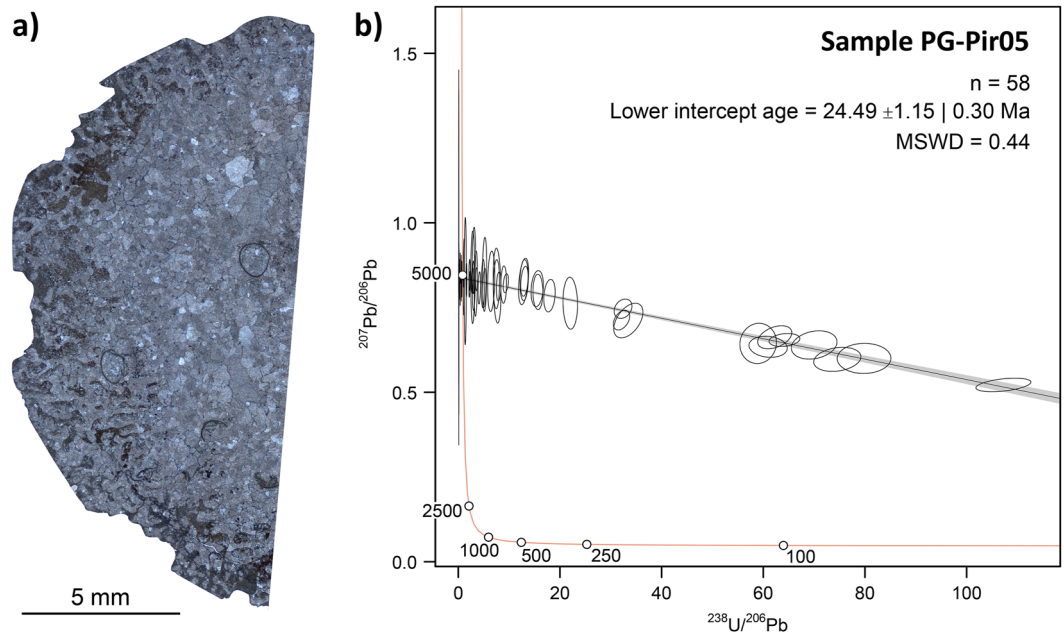

Figure 14. U-Pb calcite age of coral block from the Pirgel mud volcano. (a) Crossed-polar microscopic image. (b) Tera-Wasserburg diagram with uncertainty ellipses (2SE). A mean standard weight deviation of <1 indicates a closed system behavior (Guillong et al., 2020). See Table S5 for isotopic ratios.

prominent tuff horizon to the north (samples PG-T01/T04) is stratigraphically positioned ~430–530 m above the uppermost (youngest) sample site (PG170) of the magnetostratigraphic section (Figures 2c and 2d). Therefore, the top of the magnetostratigraphic section must be older than ~17.65–17.8 Ma (Figures 13a and 13b).

The combination of independent age constraints from U-Pb ages and the high resolution of the magnetostratigraphic section (except for Section A, Figure 9f) allow for a robust correlation of the measured MPS with the GPTS (Figure 15). Section A displays several potential reverse magnetozones characterized by only one ChRM direction, which have to be interpreted with caution. The lowermost normal magnetozone of the MPS is correlated to chron C7n, post-dating the U-Pb calcite age of the coral block. The two normal magnetozones between ~250 and 500 m of the MPS are interpreted as belonging to chron C6Cn, in accordance with the U-Pb zircon age of PG-T05 from the shallow-marine deposits of the neighboring syncline (Figure 3). Continuing up the section, the normal magnetozone with potential, but not fully resolved, reversals between ~630 and 850 m of the MPS are linked to chron C6Bn. Above, a long reversed interval is punctuated by two mixed polarity intervals at 915 and 1,060 m, interpreted as C6AAr.2n and C6AAr.1n, respectively, and by a short normal magnetozone starting at 1,380 that correlates to chron C6AAn (Figure 15). Between ~1,750 and the top of the section, three long normal magnetozones correspond to C6A and C6n normal magnetochrons. The top of the section yields an age of <19.72 Ma (base C6n), which is corroborated by the upper tuff horizon 430–530 m, located above the top of the section (Figure 15). An alternative interpretation suggesting that the topmost normal interval represents chron C5En does not align well with the underlaying MPS.

The resulting age constraint for the shallow marine-to-continental sequence of the Karvandar Basin indicates that the first shallow marine layered sediments deposited onto the chaotic shale-dominated formation in late Chattian, just before the Oligocene to Miocene boundary (Figure 15). The transition of shallow marine to continental facies occurred during the Chattian in the eastern syncline, perhaps favored by the global sea-level drop at the Ologicene-Miocene boundary (OMB, Liebrand et al., 2011). The western and southern synclines exhibit more prevalent marine sedimentation at their base, and the marine-to-continental transition, at least in the western syncline, occurred in early Aquitanian, based on U-Pb zircon ages of tuff sample PG-T05 (Figures 3 and 14). The continentalization of the eastern syncline close to the OMB is accompanied by an increase of average compacted sediment accumulation rate from ~15 to ~50 cm/kyr. Upsection, sediment accumulation rate increases constantly to reach >120 cm/kyr between ~2,200 and 2,700 m, corresponding to 20–20.5 Ma (Figure 15). After ~20 Ma, the sediment accumulation rate gradually decreases to ~50 cm/kyr near the top of the

10.1029/2023TC007971

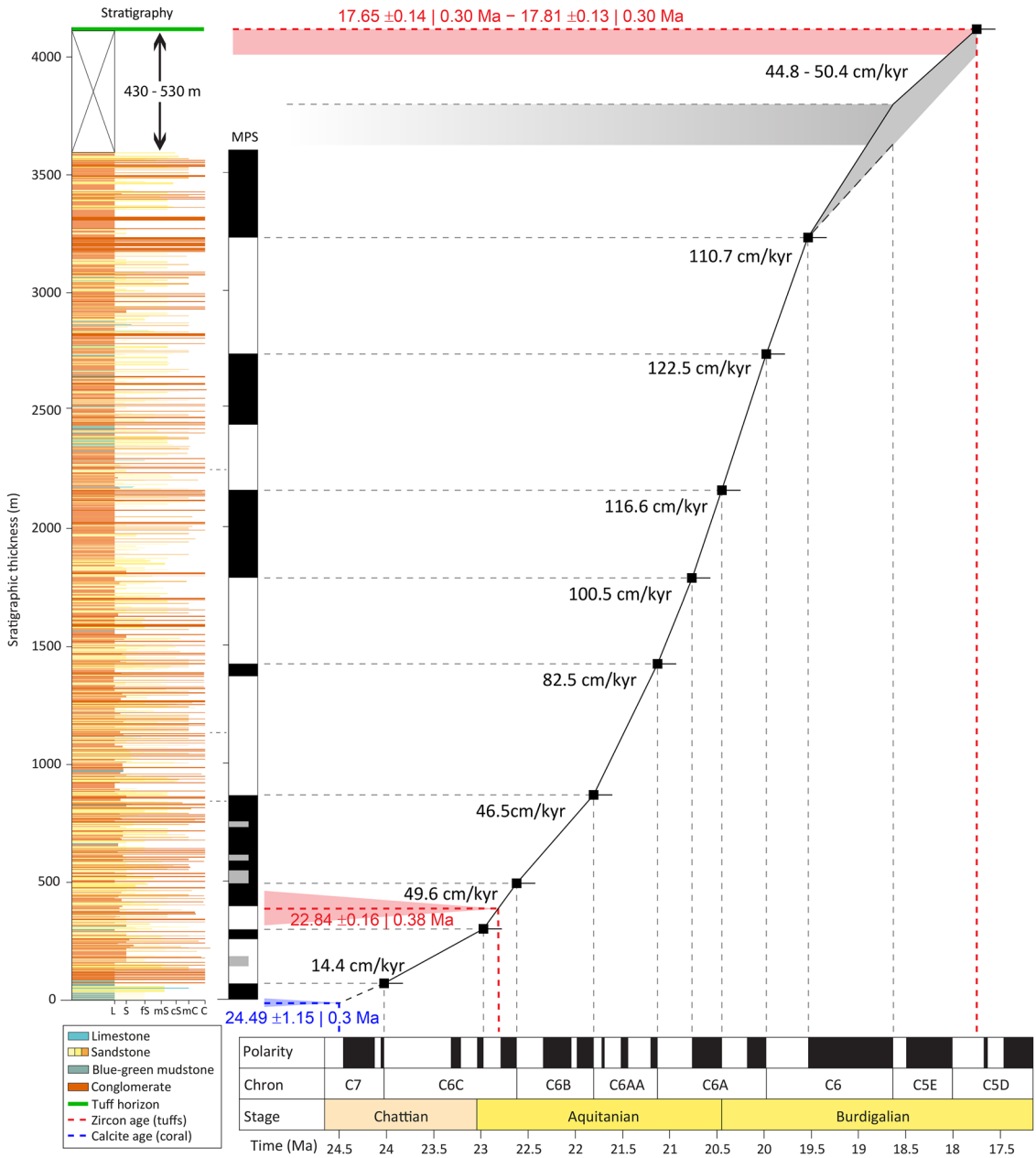

Figure 15. Correlation of the local magnetopolarity stratigraphy from the Karvandar Basin with the geomagnetic polarity timescale (Gradstein & Ogg, 2020). The correlation is anchored by the U-Pb calcite age of the coral that pre-dates the base of the section (blue dotted line) and the tuff layers at the base and above the section (red dotted lines). Shaded red indicate estimations of the position of the tuff layers with regard to the magnetostratigraphic section. Resulting sediment accumulation rates fit the observed transition from marine to continental facies. The rates of sedimentation are illustrated beside the curve in cm/kyr.

section. The magnetostratigraphy presents the irst age constraints from the Karvandar Basin and contributes to our broader understanding of the basin's geological history, providing a framework to discuss in the following the driving mechanisms behind the observed changes in sedimentation patterns.

6.2. Tectono-Stratigraphic Evolution of the Karvandar Basin

The stratigraphically lowermost (i.e., oldest) sediments in the Karvandar Basin consist of Eocene turbiditic sequences interbedded with occasional patch reefs (Figures 1 and 2). Published data on provenance analysis suggest that these turbidites are part of the Neh accretionary Complex (NAC, Figure 16a) with a dissected arc or recycled orogenic sediment source to the northeast (sample 134 in Mohammadi, Burg, and Winkler (2016)). The

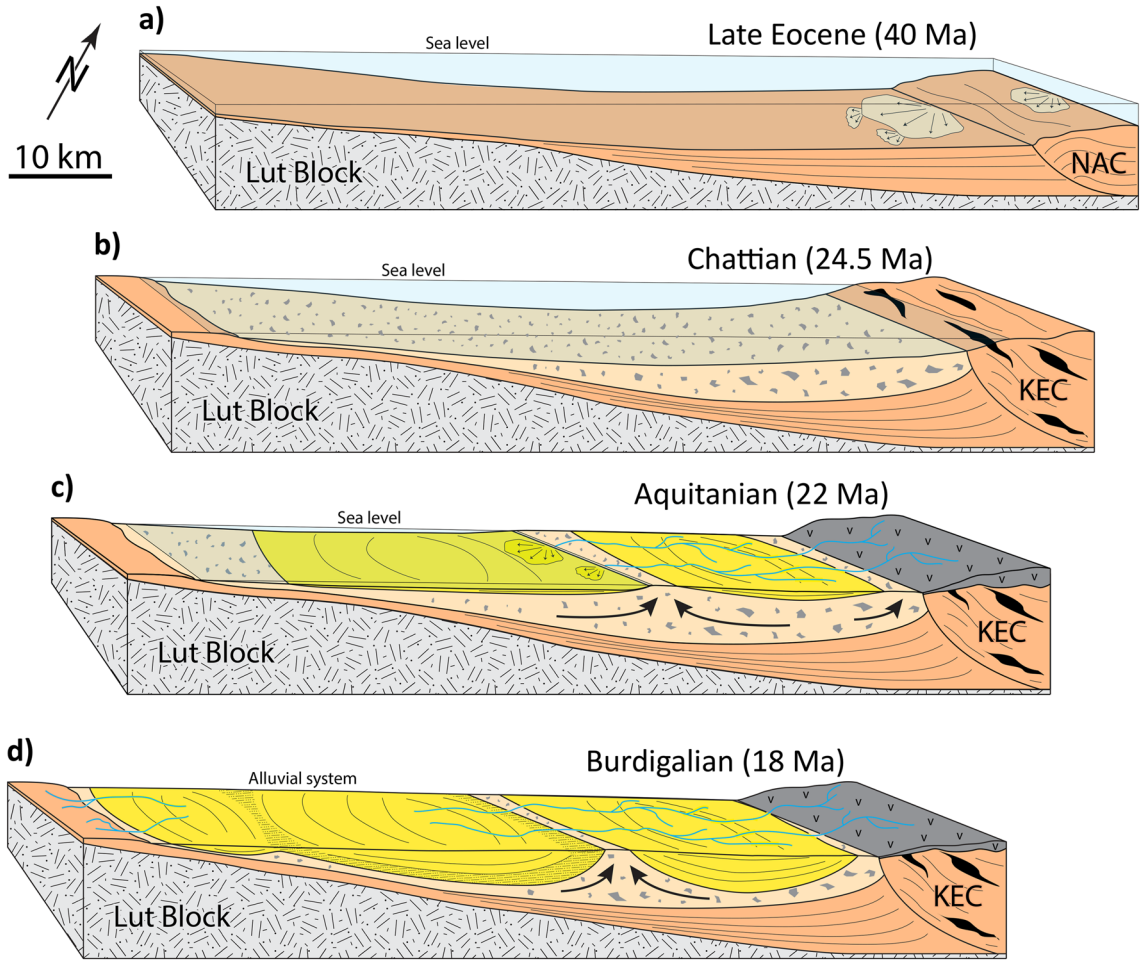

Figure 16. Schematic evolution of the Karvandar Basin from Eocene to early Miocene. (a) Pre- to syn-collisional trench deposition of typical Neh Accretionary Wedge deep-marine turbidites. (b) Emplacement of olistostrome with volcanic blocks sourced from gravitational collapse of a proximal volcano. (c) First deposition of continental sandstones and conglomerates in the east and shallow-marine facies in the west. (d) Sediment load leads to downbuilding into water-saturated, non-lithified olistostrome mass.

presence of patch reefs indicates, at least occasionally, a shallow-marine sedimentary environment (Figure 1b). During the Eocene, the region experienced potential local uplift and subsidence, which can be attributed to the onset of continental collision and subsequent lithospheric delamination along the SSZ at the corresponding latitude (Mohammadi, Burg, Bouilhol, & Ruh, 2016). Occurrences of thinned Eocene turbidites along the western edge of the Karvandar Basin suggests that the extent of the basin did not considerably change since the Eocene (Figure 16a).

Above the Eocene deposits, the lithology of the Karvandar Basin is characterized by mud-dominated sediments that separate the large-scale synclines and forms the framework of the Pirgel mud volcano (Figures 1–3). Chaotically distributed meter-size angular to sub-angular blocks of mostly volcanic origin (Figure 6c) suggest that this lithology represents an olistostrome, that is, a submarine debris flow (Figure 16b). Similar gravitationally emplaced olistostromes that traveled up to hundreds of kilometers along gently dipping slopes were reported in other regions such as the Canary Islands (Masson et al., 1998), the Gulf of Cádiz (Medialdea et al., 2004), and the Makran accretionary wedge (Burg et al., 2008). The abundance of volcanic blocks indicates that the source area was located on the slope of a volcanic edifice. The olistostrome was deposited into a shallow basin, overlaying the Eocene clastic slope sediments of the NAC (Figures 2b and 16b). Nannofossil and foraminiferal assemblages derived from the extruded mud from the Pirgel mud volcano and the U-Pb calcite age (24.49 Ma, Figure 14) of a coral block in the mud matrix (Figure 6d) suggest olistostrome emplacement in the latest Oligocene. This is corroborated by the U-Pb zircon age of 22.84 Ma obtained from

the lowermost part of the overlying sequence (Figures 3 and 13c). Besides, the occurrence of Cretaceous foraminifera can be related to the reworking of older strata, which is commonly observed in debris flow deposits.

The first layered deposits overlaying the mud-dominated lithology consist of shallow-marine shale and sandstones with asymmetric ripple marks (Figure 4a). The thickness of the marine sequence, distinguishable by its greenish color in satellite images, compared to reddish colors of the continental deposits, varies significantly from northeast to southwest within the Karvandar Basin (Figures 1–3). In the sampled section, marine deposits account for less than 100 m thickness (Figure 5a), whereas on the western side of the Pirgel mud volcano, the marine strata at the base extend to a thickness of ∼1 km (Figures 2c, 2d, and 3). A similar increase in thickness of the marine strata is observed in the eastern syncline from north to south (Figures 1b, 2a, and 2b). These variations in marine strata thickness indicate that a shallow sea opened toward the southwest during earliest Miocene (Figure 16c). The measured paleocurrents within the Karvandar Basin further support this interpretation, indicating sediment transport from northeast to southwest, or east-northeast to west-southwest for a counter clock-wise rotated Karvandar Basin (Figures 12a and 12b). Furthermore, the distinct difference in marine strata thickness at the base of the western and eastern synclines along the mud-dominated lithology hosting the Pirgel mud volcano suggests that this ridge already existed in early Miocene, forming the coastline (Figure 16c).

During the latest Aquitanian (∼20.5 Ma), the Karvandar Basin underwent a phase of aggradational continental sedimentation (Figure 16d), indicated by the presence of interlayered redbeds and amalgamated conglomerates (Figures 4b and 4c). Sandstone framework data along the investigated section do not indicate any significant changes in sediment sources supplying the Karvandar Basin (Figures 5c–5e). The basin experienced consistently high sediment accumulation rates of ∼100 cm/kyr, extending at least until the end of the Burdigalian stage (Figure 15). Based on these observations, we propose that the consistent depositional environment in the Karvandar Basin reflects a balance between local subsidence and sediment accumulation, related to downbuilding of the synclines into the underlaying olistostrome (Figure 16d). This interpretation is consistent with an early existence of a mud ridge between the synclines, the general absence of major anticlines throughout the Karvandar Basin and the detection of syn-tectonic sedimentary onlaps and growth strata (Figure 2). In this sense, the mud ridge represents an elongated diapiric structure induced by the density contrast of the fluid-saturated olistostrome mass and the rapidly accumulating overlying continental sequence (Figure 16d). The Pirgel mud volcano pinches through this diapiric structure and fluids from the overpressures mud lithology are released.

Gravity-driven minibasins (or withdrawal basins) are traditionally linked to salt tectonics (Hudec et al., 2009; Jackson & Talbot, 1991). However, recent studies reported depositional minibasins downbuilding into poorly compacted and fluid-saturated sedimentary mélanges of low bulk viscosity and density (Chang et al., 2019; Dinc et al., 2022; Ruh et al., 2018). In particular, several observations reveal the similarity between the synclines of the Karvandar Basin and sub-circular shale-related minibasins of the Makran, SE Iran (Ruh et al., 2018): (a) Sedimentary sequences are very thick and represent shallow-marine deposits (e.g., Dolati, 2010; McCall, 1997; Sahandi, 1996); (b) Mud lithologies underlying these sequences are interpreted to represent mobilized olistostrome deposits (Burg et al., 2008) that extrude in mud volcanoes (Babadi et al., 2019); (c) Dish-shaped synclines exhibit growth strata patterns, indicating syn-tectonic sediment accumulation; and (d) Anticlines are generally absent and synclines are either welded against each other or are separated by diapiric mud ridges (Figures 1–3 and 16).

After deposition of the clastic sequence related to the erosion of the volcanic arc, the minibasin synclines of the Karvandar Basin most probably underwent a phase of fold tightening, as E-W-oriented compression has been reported to affect the SSZ until late Miocene (Jentzer et al., 2017). Furthermore, mean magnetic directions with a declination of 328° indicate a counter-clockwise (CCW) rotation of the Karvandar Basin of ∼30° since its deposition, because the apparent polar wander path of Eurasia only provides a deviation between 1.31° and 2.64° since the last 20 Myr (Besse & Courtillot, 2002; Torsvik et al., 2012). Walker and Jackson (2004) interpreted several strike-slip fault systems in East Iran to have been responsible for CCW block rotation of 10–25°. They related this block rotation to 75–105 km of right-lateral shear in East Iran since ∼5–7 Ma. Furthermore, Mattei et al. (2012) reported CCW rotations of up to 35° in Oligocene-Miocene sedimentary rocks from Central Iran, related to large-scale right-lateral strike-slip systems. This supports that vertical-axis rotation of the Karvandar Basin is related to regional tectonics along the East Iranian strike-slip system and that rotation occurred after the deposition of the clastic sequence.

6.3. Regional Tectonic Implications

The late Oligocene to early Miocene marine strata of the Karvandar Basin were deposited in a shallow sea extending toward the southwest of the investigated area. Previous studies suggested that the westward extension of this shallow sea (today Jaz Murian Depression, Figure 1a) resulted from local uplift related to the imbrication of the North Makran toward the south during the Late Cretaceous to Eocene (McCall, 1997; Shahabpour, 2010). The Jaz Murian Depression remained a shallow sea until at least the early Miocene, as evidenced by the shallow-marine reefal limestones and clastic deposits of the Karvandar Basin (Ghorashi & Vaezipour, 1987; McCall, 1997; McCall & Eftekhar Nezhad, 1994; McCall et al., 1994; this study). Furthermore, extensive provenance analysis points toward the abandonment of the Cretaceous arc south of the Jaz Murian and the formation of a new arc, probably the eastward continuation of the Urumieh-Dokhtar arc in the Zargos (e.g., Alavi, 1994; Farhoudi & Karig, 1977; M. R. Hosseini et al., 2017), north of the Jaz Murian in the Eocene (Mohammadi, Burg, Winkler, et al., 2016; Mohammadi et al., 2017). This implies a transition of the Jaz Murian Depression from a backarc to a forearc basin during the early Paleogene.

As outlined above, the Karvandar Basin was probably connected to the Jaz Murian shallow sea in early Miocene. However, several key features suggest that the Karvandar Basin also functions as a Molasse-type foreland basin to the SSZ. These features include the large-scale structural disposition sub-parallel to the Karvandar Fault, the tectono-stratigraphic composition of the South Sistan (Figure 1a), and paleocurrents indicating sediment transport from the northeast to the southwest (Figure 12). Taking into consideration a CCW rotation of the basin since the late Miocene, paleocurrents indicate an east-northeast-west-southwest sediment transport, perpendicular to the Karvandar Fault (Figures 12a and 12b). The creation of new accommodation space in the foreland of the SSZ resulting in the formation of the Karvandar Basin is not trivial, as the continental sequence post-dates SSZ collision for ~10–15 Myr (Jentzer et al., 2022; Mohammadi, Burg, Bouilhol, & Ruh, 2016; Tirrul et al., 1983). One possible explanation for this delayed response is the reported post-collisional westward-propagating lithospheric delamination (Mohammadi, Burg, Bouilhol, & Ruh, 2016). Similar effects of mantle deformation on the evolution of foreland basins were documented in the Swiss Molasse Basin, where processes such as slab rollback and plate bending provided additional accommodation space without significant changes in surface topography (Schlunegger & Kissling, 2015). Additionally, slab breakoff may have resulted in delayed isostatic rebound and increased sediment fluxes (Schlunegger & Castelltort, 2016).

Sandstone and microconglomerate framework of the Karvandar sequence consisting mainly of andesitic-basaltic volcanic rock fragments (Figures 5c–5e and 10a, Figures S4–S6 in Supporting Information S1) indicate a homogeneous and continuous sediment source of volcanic rocks, with subordinate contributions from ophiolitic and metamorphic source rocks. These sediments were likely eroded from an active volcanic arc and an uplifted subduction complex (Figures 10b and 10c, Dickinson, 1985; Dickinson & Suczek, 1979). Comparison to the more mature clastic deposits of the South Sistan Basin (Mohammadi, Burg, & Winkler, 2016) indicate a primary volcanic source without reworking of the Sistan turbidites (Figure 10). Furthermore, up to ~25-m-thick tuff layers (Figures 2c and 2d) suggest that the Karvandar Basin was filled in the proximity of active volcanism. We interpret that a volcanic system, possibly located to the northeast, served as the source of the volcanic blocks in the late Oligocene olistostrome, as well as the tuff layers at the base and the top of the sequence, and the clastic sequence itself. Magmatism of similar age has been reported from the Mirabad pluton ~70 km to the northeast (~19 Ma, Pang et al., 2014) and the Bazman volcanic complex (~21.7 Ma, Sholeh et al., 2016) to the west of the Karvandar Basin. Trace element ratios from the Mirabad pluton indicate a subduction-related mantle source, similar to the nearby Taftan volcano, which forms the recent Makran magmatic arc together with the Bazman volcano to the west and the Koh-i-Soltan volcano to the east (Pang et al., 2014).

Based on our age constraints and framework analysis of the shallow-marine to continental upper Oligocene to lower Miocene sequence within the Karvandar Basin, we propose that active volcanism related to arc magmatism of the northward-directed Makran subduction zone initiated in the region of Mirabad and present-day Taftan volcano no later than in the late Aquitanian, at 24.5 Ma, when a gravitational collapse of a volcano flank occurred, resulting in the emplacement of the Karvandar olistostrome (Figure 16b). The volcanic activity persisted until at least until 17.7 Ma (Figure 13a), indicated by the presence of thick tuff layers within the Karvandar Basin, suggesting a nearby source. It is likely that volcanic rocks covered extensive areas surrounding the Taftan volcano (Aghanabati et al., 1994), considering the first-cycle nature of the investigated sandstone framework. This finding excludes potential recycling of clastic rocks from the NAC.

7. Conclusions

We conducted magnetostratigraphy and sandstone framework of the clastic shallow-marine to continental sequence of the Karvandar Basin, a peripheral foreland basin of the South SSZ. We draw the following conclusions from the interpretation of the multidisciplinary results presented in this study:

- The magnetostratigraphic section, anchored to the GPTS by U-Pb zircon ages of interlayered tuffs, reveals a late Oligocene to early Miocene depositional age of the Karvandar sequence (~24–18 Ma).
- First-cycle volcanic nature of the sandstone framework and the occurrence of up to 25-m-thick tuff layers indicate syn-sedimentary active volcanism during the deposition of the Karvandar Basin.
- The mud-dominated lithology underlying the clastic sequence is interpreted to represent an olistostrome sourced from a volcanic flank, based on the occurrence of randomly oriented centimeter- to meter-sized angular to sub-angular blocks of volcanic origin.
- A calcite U-Pb age of a coral block in the olistostrome indicates an emplacement age of 24.5 ± 1.3 Ma.
- Angular unconformities, the absence of anticlines, and significant thickness variations of the marine strata across mud ridges suggest early mud diapirism and gravity-driven minibasin downbuilding into the olistostrome.
- Subduction-related magmatic intrusions of early Miocene age toward the northeast of the Karvandar Basin with geochemical signatures similar to the quaternary Taftan volcano indicate that magmatic arc volcanism related to the Makran subduction zone started in latest Oligocene and represents the source of the volcanic blocks in the olistostrome and Karvandar clastic sequence and tuffs.

Data Availability Statement

All isotopic, fossil, sandstone petrological and paleomagnetic data used for to constrain the magnetostratigraphy in the study are available in Supporting Information S1 and at the ETH Research Collection via https://doi.org/10.3929/ethz-b-000636892 in copyright—non-commercial use permitted (Ruh et al., 2023).

Acknowledgments
The authors would like to thank the Associate Editor and two anonymous Reviewers for their detailed and constructive comments, significantly improving the quality of the manuscript. We acknowledge support of the publication fee by the CSIC Open Access Publication Support Initiative through its Unit of Information Resources for Research (URICI). JBR is supported by a Ramón y Cajal scholarship (RYC2021-031331-I) funded by the Spanish Ministry of Science and Innovation.

References

Aghanabati, A., Sahandi, M. R., Mohajjel, M., & Hajmollah Ali, A. (1994). Geological map of the Khash quadrangle.

Agnini, C., Fornaciari, E., Raffi, I., Catanzariti, R., Pälike, H., Backman, J., & Rio, D. (2014). Biozonation and biochronology of Paleogene calcareous nannofossils from low and middle latitudes. *Newsletters on Stratigraphy*, *47*(2), 131–181. https://doi.org/10.1127/0078-0421/2014/0042

Alavi, M. (1994). Tectonics of the Zagros orogenic belt of Iran - New data and interpretations. *Tectonophysics*, *229*(3–4), 211–238. https://doi.org/10.1016/0040-1951(94)90030-2

Alavi, M. (2007). Structures of the Zagros fold-thrust belt in Iran. *American Journal of Science*, *307*(9), 1064–1095. https://doi.org/10.2475/09.2007.02

Allen, P. A., Crampton, S. L., & Sinclair, H. D. (1991). The inception and early evolution of the North Alpine foreland basin, Switzerland. *Basin Research*, *3*(3), 143–163. https://doi.org/10.1111/j.1365-2117.1991.tb00124.x

Allen, P. A., & Homewood, P. (2009). *Foreland basins*. John Wiley & Sons.

Angiboust, S., Agard, P., De Hoog, J. C. M., Omrani, J., & Plunder, A. (2013). Insights on deep, accretionary subduction processes from the Sistan ophiolitic "melange" (Eastern Iran). *Lithos*, *156*, 139–158. https://doi.org/10.1016/j.lithos.2012.11.007

Arjmandzadeh, R., Karimpour, M. H., Mazaheri, S. A., Santos, J. F., Medina, J. M., & Homam, S. M. (2011). Sr-Nd isotope geochemistry and petrogenesis of the Chah-Shaljami granitoids (Lut Block, Eastern Iran). *Journal of Asian Earth Sciences*, *41*(3), 283–296. https://doi.org/10.1016/j.jseaes.2011.02.014

Babadi, M. F., Mehrabi, B., Tassi, F., Cabassi, J., Vaselli, O., Shakeri, A., et al. (2019). Origin of fluids discharged from mud volcanoes in SE Iran. *Marine and Petroleum Geology*, *106*, 190–205. https://doi.org/10.1016/j.marpetgeo.2019.05.005

Babazadeh, S. A., & De Wever, P. (2004). Early Cretaceous radiolarian assemblages from radiolarites in the Sistan Suture (eastern Iran). *Geodiversitas*, *26*(2), 185–206.

Backman, J., Raffi, I., Rio, D., Fornaciari, E., & Pälike, H. (2012). Biozonation and biochronology of Miocene through Pleistocene calcareous nannofossils from low and middle latitudes. *Newsletters on Stratigraphy*, *45*(3), 221–244. https://doi.org/10.1127/0078-0421/2012/0022

Bagheri, S., & Damani Gol, S. (2020). The eastern Iranian orocline. *Earth-Science Reviews*, *210*, 103322. https://doi.org/10.1016/j.earscirev.2020.103322

Berberian, F., Muir, I. D., Pankhurst, R. J., & Berberian, M. (1982). Late cretaceous and early Miocene Andean-type plutonic activity in northern Makran and Central Iran. *Journal of the Geological Society*, *139*(Sep), 605–614. https://doi.org/10.1144/gsjgs.139.5.0605

Berberian, M., Jackson, J. A., Qorashi, M., Khatib, M. M., Priestley, K., Talebian, T., & Ghafuri-Ashtiani, M. (1999). The 1997 may 10 Zirkuh (Qa'enat) earthquake (M-w 7.2): Faulting along the Sistan suture zone of eastern Iran. *Geophysical Journal International*, *136*(3), 671–694. https://doi.org/10.1046/j.1365-246x.1999.00762.x

Berberian, M., Jackson, J. A., Qorashi, M., Talebian, M., Khatib, M., & Priestley, K. (2000). The 1994 Sefidabeh earthquakes in eastern Iran: Blind thrusting and bedding-plane slip on a growing anticline, and active tectonics of the Sistan suture zone. *Geophysical Journal International*, *142*(2), 283–299. https://doi.org/10.1046/j.1365-246x.2000.00158.x

Besse, J., & Courtillot, V. (2002). Apparent and true polar wander and the geometry of the geomagnetic field over the last 200 Myr. *Journal of Geophysical Research*, *107*(B11). EPM-6. https://doi.org/10.1029/2000jb000050

Beydokhti, R. M., Karimpour, M. H., Mazaheri, S. A., Santos, J. F., & Klotzli, U. (2015). U-Pb zircon geochronology, Sr-Nd geochemistry, petrogenesis and tectonic setting of Mahoor granitoid rocks (Lut Block, Eastern Iran). *Journal of Asian Earth Sciences*, *111*, 192–205. https://doi.org/10.1016/j.jseaes.2015.07.028

Bown, P. R., & Young, J. (1998). Introduction. In P. R. Bown (Ed.), *Calcareous nannofossil biostratigraphy* (pp. 1–15). Kluwer Academic.

Bröcker, M., Hövelkröger, Y., Rad, G. F., Berndt, J., Scherer, E. E., Kurzawa, T., & Moslempour, M. E. (2022). The magmatic and tectono-metamorphic history of the Sistan suture zone, Iran: New insights into a key region for the convergence between the Lut and Afghan blocks. *Journal of Asian Earth Sciences*, *236*, 105313. https://doi.org/10.1016/j.jseaes.2022.105313

Bröcker, M., Rad, G. F., Burgess, R., Theunissen, S., Paderin, I., Rodionov, N., & Salimi, Z. (2013). New age constraints for the geodynamic evolution of the Sistan Suture Zone, eastern Iran. *Lithos*, *170*, 17–34. https://doi.org/10.1016/j.lithos.2013.02.012

Burg, J. P. (2018). Geology of the onshore Makran accretionary wedge: Synthesis and tectonic interpretation. *Earth-Science Reviews*, *185*, 1210–1231. https://doi.org/10.1016/j.earscirev.2018.09.011

Burg, J. P., Bernoulli, D., Smit, J., Dolati, A., & Bahroudi, A. (2008). A giant catastrophic mud-and-debris flow in the Miocene Makran. *Terra Nova*, *20*(3), 188–193. https://doi.org/10.1111/j.1365-3121.2008.00804.x

Carrapa, B., Di Giulio, A., Mancin, N., Stockli, D., Fantoni, R., Hughes, A., & Gupta, S. (2016). Tectonic significance of Cenozoic exhumation and foreland basin evolution in the Western Alps. *Tectonics*, *35*(8), TC004132–1912. https://doi.org/10.1002/2016tc004132

Chadima, M. (2006). Remasoft 3.0 a user-friendly paleomagnetic data browser and analyzer. *Travaux Géophysiques*, *27*, 20.

Chang, S. P., Jamaludin, S. N. F., Pubellier, M., Zainuddin, N. M., & Choong, C. M. (2019). Collision, melange and circular basins in north Borneo: A genetic link? *Journal of Asian Earth Sciences*, *181*, 103895. https://doi.org/10.1016/j.jseaes.2019.103895

Chapman, J. B., Carrapa, B., DeCelles, P. G., Worthington, J., Mancin, N., Cobianchi, M., et al. (2020). The Tajik Basin: A composite record of sedimentary basin evolution in response to tectonics in the Pamir. *Basin Research*, *32*(3), 525–545. https://doi.org/10.1111/bre.12381

Dal Zilio, L., Kissling, E., Gerya, T., & Dinther, Y. (2020). Slab rollback orogeny model: A test of concept. *Geophysical Research Letters*, *47*(18), e2020GL089917. https://doi.org/10.1029/2020gl089917

Davidson, S. K., Hartley, A. J., Weissmann, G. S., Nichols, G. J., & Scuderi, L. A. (2013). Geomorphic elements on modern distributive fluvial systems. *Geomorphology*, *180*, 82–95. https://doi.org/10.1016/j.geomorph.2012.09.008

Davoudzadeh, M. (1997). Iran. In *Encyclopedia of European and Asian regional geology* (pp. 384–405). Springer Netherlands.

DeCelles, P. G., Gehrels, G. E., Najman, Y., Martin, A. J., Carter, A., & Garzanti, E. (2004). Detrital geochronology and geochemistry of Cretaceous-Early Miocene strata of Nepal: Implications for timing and diachroneity of initial Himalayan orogenesis. *Earth and Planetary Science Letters*, *227*(3–4), 313–330. https://doi.org/10.1016/j.epsl.2004.08.019

DeCelles, P. G., & Giles, K. A. (1996). Foreland basin systems. *Basin Research*, *8*(2), 105–123. https://doi.org/10.1046/j.1365-2117.1996.01491.x

Delavari, M., Amini, S., Schmitt, A. K., McKeegan, K. D., & Harrison, T. M. (2014). U–Pb geochronology and geochemistry of Bibi-Maryam pluton, eastern Iran: Implication for the late stage of the tectonic evolution of the Sistan Ocean. *Lithos*, *200*, 197–211. https://doi.org/10.1016/j.lithos.2014.04.015

Dickinson, W. R. (1985). Interpreting provenance relations from detrital modes of sandstones. In G. G. Zuffa (Ed.), *Provenance of arenites* (Vol. 148, pp. 333–361). Springer.

Dickinson, W. R., & Suczek, C. A. (1979). Plate-tectonics and sandstone compositions. *Aapg Bulletin-American Association of Petroleum Geologists*, *63*(12), 2164–2182.

Dinc, G., Callot, J.-P., & Ringenbach, J.-C. (2022). Shale mobility: From salt-like shale flow to fluid mobilization in gravity-driven deformation, the late Albian–Turonian White Pointer Delta (Ceduna Subbasin, Great Bight, Australia). *Geology*, *51*(2), 174–178. https://doi.org/10.1130/g050611.1

Dolati, A. (2010). *Stratigraphy, structural geology and low-temperature thermochronology across the Makran accretionary wedge in Iran* (PhD), Eidgenössische Technische Hochschule (ETH) Zürich (p. 19151).

Etemad-Saeed, N., Najafi, M., & Vergés, J. (2020). Provenance evolution of Oligocene–Pliocene foreland deposits in the Dezful embayment to constrain Central Zagros exhumation history. *Journal of the Geological Society*, *177*(4), 799–817. https://doi.org/10.1144/jgs2019-206

Farhoudi, G., & Karig, D. E. (1977). Makran of Iran and Pakistan as an active arc system. *Geology*, *5*(11), 664–668. https://doi.org/10.1130/0091-7613(1977)5<664:MOIAPA>2.0.CO;2

Fisher, R. A. (1953). Dispersion on a sphere. *Proceedings of the Royal Society of London. Series A. Mathematical Physical Sciences*, *217*(1130), 295–305. https://doi.org/10.1098/rspa.1953.0064

Folk, R. L. (1980). *Petrology of sedimentary rocks*. Hemphill Publishing Company.

Freund, R. (1970). Rotation of strike slip faults in Sistan, Southeast-Iran. *The Journal of Geology*, *78*(2), 188–200. https://doi.org/10.1086/627500

Garcés, M. (2015). Magnetostratigraphic dating. In W. Jack Rink & J. W. Thompson (Eds.), *Encyclopedia of scientific dating methods. Encyclopedia of Earth sciences series*. Springer.

Garcés, M., López-Blanco, M., Valero, L., Beamud, E., Muñoz, J. A., Oliva-Urcia, B., et al. (2020). Paleogeographic and sedimentary evolution of the South Pyrenean foreland basin. *Marine and Petroleum Geology*, *113*, 104105. https://doi.org/10.1016/j.marpetgeo.2019.104105

Garefalakis, P., & Schlunegger, F. (2019). Tectonic processes, variations in sediment flux, and eustatic sea level recorded by the 20 Myr old Burdigalian transgression in the Swiss Molasse basin. *Solid Earth*, *10*(6), 2045–2072. https://doi.org/10.5194/se-10-2045-2019

Ghorashi, M., & Vaezipour, M. J. (1987). Geological map of the Karvandar quadrangle.

Gradstein, F. M., & Ogg, J. G. (2020). The chronostratigraphic scale. In *Geologic time scale 2020* (pp. 21–32). Elsevier.

Guillong, M., von Quadt, A., Sakata, S., Peytcheva, I., & Bachmann, O. (2014). LA-ICP-MS Pb-U dating of young zircons from the Kos-Nisyros volcanic centre, SE Aegean arc. *Journal of Analytical Atomic Spectrometry*, *29*(6), 963–970. https://doi.org/10.1039/c4ja00009a

Guillong, M., Wotzlaw, J.-F., Looser, N., & Laurent, O. (2020). Evaluating the reliability of U–Pb laser ablation inductively coupled plasma mass spectrometry (LA-ICP-MS) carbonate geochronology: Matrix issues and a potential calcite validation reference material. *Geochronology*, *2*(1), 155–167. https://doi.org/10.5194/gchron-2-155-2020

Hartley, A. J., Weissmann, G. S., Nichols, G. J., & Warwick, G. L. (2010). Large distributive fluvial systems: Characteristics, distribution, and controls on development. *Journal of Sedimentary Research*, *80*(1–2), 167–183. https://doi.org/10.2110/jsr.2010.016

Hayward, B. W., Le Coze, F., Vachard, D., & Gross, O. (2022). World foraminifera database: 545. Retrieved from http://www.marinespecies.org/foraminifera

Horstwood, M. S. A., Kosler, J., Gehrels, G., Jackson, S. E., McLean, N. M., Paton, C., et al. (2016). Community-derived standards for LA-ICP-MS U-(Th-)Pb geochronology - Uncertainty propagation, age interpretation and data reporting. *Geostandards and Geoanalytical Research*, *40*(3), 311–332. https://doi.org/10.1111/j.1751-908x.2016.00379.x

Hosseini, M. R., Hassanzadeh, J., Alirezaei, S., Sun, W. D., & Li, C. Y. (2017). Age revision of the Neotethyan arc migration into the southeast Urumieh-Dokhtar belt of Iran: Geochemistry and U-Pb zircon geochronology. *Lithos*, *284*, 296–309. https://doi.org/10.1016/j.lithos.2017.03.012

Hosseini, Z., & Afsharianzadeh, A. M. (1993). Geological map of the Ziruki-ye-Goharkuh quadrangle.
Huber, H. (1978). Geological map of Iran.
Hudec, M. R., Jackson, M. P. A., & Schttltz-Ela, D. D. (2009). The paradox of minibasin subsidence into salt: Clues to the evolution of crustal basins. *Geological Society of America Bulletin*, *121*(1–2), 201–221. https://doi.org/10.1130/b26275.1
Huerta, P., Armenteros, I., & Silva, P. G. (2011). Large-scale architecture in non-marine basins: The response to the interplay between accommodation space and sediment supply. *Sedimentology*, *58*(7), 1716–1736. https://doi.org/10.1111/j.1365-3091.2011.01231.x
Hunziker, D., Burg, J. P., Bouilhol, P., & von Quadt, A. (2015). Jurassic rifting at the Eurasian Tethys margin: Geochemical and geochronological constraints from granitoids of North Makran, southeastern Iran. *Tectonics*, *34*(3), 571–593. https://doi.org/10.1002/2014tc003768
Ingersoll, R. V., Bullard, T. F., Ford, R. L., Grimm, J. P., Pickle, J. D., & Sares, S. W. (1984). The effect of grain-size on Detrital modes - A test of the Gazzi-Dickinson point-counting method. *Journal of Sedimentary Petrology*, *54*(1), 103–116.
Jackson, M., & Talbot, C. J. (1991). A glossary of salt tectonics.
Jentzer, M., Agard, P., Bonnet, G., Monié, P., Fournier, M., Whitechurch, H., et al. (2022). The North Sistan orogen (Eastern Iran): Tectono-metamorphic evolution and significance within the Tethyan realm. *Gondwana Research*, *109*, 460–492. https://doi.org/10.1016/j.gr.2022.04.004
Jentzer, M., Fournier, M., Agard, P., Omrani, J., Khatib, M. M., & Whitechurch, H. (2017). Neogene to Present paleostress field in Eastern Iran (Sistan belt) and implications for regional geodynamics. *Tectonics*, *36*(2), 321–339. https://doi.org/10.1002/2016tc004275
Kennedy, A. K., Wotzlaw, J. F., Schaltegger, U., Crowley, J. L., & Schmitz, M. (2014). Eocene zircon reference material for microanalysis of U-Th-Pb isotopes and trace elements. *The Canadian Mineralogist*, *52*(3), 409–421. https://doi.org/10.3749/canmin.52.3.409
Kirschvink, J. (1980). The least-squares line and plane and the analysis of palaeomagnetic data. *Geophysical Journal International*, *62*(3), 699–718. https://doi.org/10.1111/j.1365-246x.1980.tb02601.x
Kopf, A. J. (2002). Significance of mud volcanism. *Reviews of Geophysics*, *40*(2), 2-1–2-52. https://doi.org/10.1029/2000rg000093
Lease, R. O., Burbank, D. W., Hough, B., Wang, Z. C., & Yuan, D. Y. (2012). Pulsed Miocene range growth in northeastern Tibet: Insights from Xunhua Basin magnetostratigraphy and provenance. *Geological Society of America Bulletin*, *124*(5–6), 657–677. https://doi.org/10.1130/b30524.1
Lechmann, A., Burg, J. P., Ulmer, P., Mohammadi, A., Guillong, M., & Faridi, M. (2018). From Jurassic rifting to Cretaceous subduction in NW Iranian Azerbaijan: Geochronological and geochemical signals from granitoids. *Contributions to Mineralogy and Petrology*, *173*(12), 102. https://doi.org/10.1007/s00410-018-1532-8
Liebrand, D., Lourens, L. J., Hodell, D. A., De Boer, B., Van de Wal, R. S. W., & Pälike, H. (2011). Antarctic ice sheet and oceanographic response to eccentricity forcing during the early Miocene. *Climate of the Past*, *7*(3), 869–880. https://doi.org/10.5194/cp-7-869-2011
Ludwig, K. R. (2003). *User's manual for isoplot 3.00, a geochronlogical toolkit for microsoft excel*. Berkeley Geochronl. Cent. Spec. Publ. (Vol. 4, pp. 25–32).
Mancin, N., Barbieri, C., Di Giulio, A., Fantoni, R., Marchesini, A., Toscani, G., & Zanferrari, A. (2016). The Friulian-Venetian Basin II: Paleogeographic evolution and subsidence analysis from micropaleontological constraints. *Italian Journal of Geosciences*, *135*(3), 460–473. https://doi.org/10.3301/ijg.2015.34
Mancin, N., Di Giulio, A., & Cobianchi, M. (2009). Tectonic vs. climate forcing in the Cenozoic sedimentary evolution of a foreland basin (Eastern Southalpine system, Italy). *Basin Research*, *21*(6), 799–823. https://doi.org/10.1111/j.1365-2117.2009.00402.x
Masson, D. G., Canals, M., Alonso, B., Urgeles, R., & Huhnerbach, V. (1998). The canary debris flow: Source area morphology and failure mechanisms. *Sedimentology*, *45*(2), 411–432. https://doi.org/10.1046/j.1365-3091.1998.0165f.x
Mattei, M., Cifelli, F., Muttoni, G., Zanchi, A., Berra, F., Mossavvari, F., & Eshraghi, S. A. (2012). Neogene block rotation in central Iran: Evidence from paleomagnetic data. *Bulletin*, *124*(5–6), 943–956. https://doi.org/10.1130/b30479.1
McCall, G. J. H. (1997). The geotectonic history of the Makran and adjacent areas of southern Iran. *Journal of Asian Earth Sciences*, *15*(6), 517–531. https://doi.org/10.1016/s0743-9547(97)00032-9
McCall, G. J. H., & Eftekhar Nezhad, J. (1994). Explanatory text of the Saravan quadrangle map (1:250,000).
McCall, G. J. H., Rosen, B., & Darrell, J. (1994). Carbonate deposition in accretionary prism settings: Early Miocene coral limestones and corals of the Makran mountain range in Southern Iran. *Facies*, *31*(1), 141–177. https://doi.org/10.1007/bf02536938
McFadden, P. L., & McElhinny, M. W. (1990). Classification of the reversal test in palaeomagnetism. *Geophysical Journal International*, *103*(3), 725–729. https://doi.org/10.1111/j.1365-246x.1990.tb05683.x
Medialdea, T., Vegas, R., Somoza, L., Vazquez, J. T., Maldonado, A., Diaz-Del-Rio, V., et al. (2004). Structure and evolution of the "Olistostrome" complex of the Gibraltar Arc in the Gulf of Cadiz (eastern Central Atlantic): Evidence from two long seismic cross-sections. *Marine Geology*, *209*(1–4), 173–198. https://doi.org/10.1016/j.margeo.2004.05.029
Moghadam, H. S., Whitechurch, H., Rahgoshay, M., & Monsef, I. (2009). Significance of Nain-Baft ophiolitic belt (Iran): Short-lived, transtensional Cretaceous back-arc oceanic basins over the Tethyan subduction zone. *Comptes Rendus Geoscience*, *341*(12), 1016–1028. https://doi.org/10.1016/j.crte.2009.06.011
Mohammadi, A., Burg, J. P., Bouilhol, P., & Ruh, J. (2016). U-Pb geochronology and geochemistry of Zahedan and Shah Kuh plutons, southeast Iran: Implication for closure of the South Sistan suture zone. *Lithos*, *248*, 293–308. https://doi.org/10.1016/j.lithos.2016.02.003
Mohammadi, A., Burg, J. P., & Guillong, M. (2022). The Siah Cheshmeh-Khoy-Misho-Tabriz fault (NW Iran) is a cryptic neotethys suture: Evidence from detrital zircon geochronology, Hf isotopes, and provenance analysis. *International Geology Review*, *64*(2), 182–202. https://doi.org/10.1080/00206814.2020.1845992
Mohammadi, A., Burg, J. P., Guillong, M., & von Quadt, A. (2017). Arc magmatism witnesses by detrial zircon U-Pb geochronology, Hf isotopes and provenance analysis of Late Cretaceous-Miocene sandstones of onshore western Makran (SE Iran). *American Journal of Science*, *317*(8), 941–964. https://doi.org/10.2475/08.2017.03
Mohammadi, A., Burg, J.-P., Ruh, J. B., & Spezzaferri, S. (2023). Clastic carbonates in the South Sistan Basin (SE Iran): Implications for subduction vergence and timing of collision. *International Geology Review*, 1–13. https://doi.org/10.1080/00206814.2023.2191119
Mohammadi, A., Burg, J. P., & Winkler, W. (2016). Detrital zircon and provenance analysis of Eocene-Oligocene strata in the South Sistan suture zone, southeast Iran: Implications for the tectonic setting. *Lithosphere*, *8*(6), 615–632. https://doi.org/10.1130/l538.1
Mohammadi, A., Burg, J. P., Winkler, W., Ruh, J., & von Quadt, A. (2016). Detrital zircon and provenance analysis of Late Cretaceous-Miocene onshore Iranian Makran strata: Implications for the tectonic setting. *Geological Society of America Bulletin*, *128*(9–10), 1481–1499. https://doi.org/10.1130/b31361.1
Mohammadi, A., Kaveh-Firouz, A., Cai, F., Dolati, A., Lom, N., & Şengör, A. C. (2023). Migration of the Palaeozoic magmatic front from Zagros to Alborz mountains with progressive closure of the Palaeo-Tethys Ocean; Insights from Zagros detrital zircon UPb age and Hf isotopic composition. *Tectonophysics*, *849*, 229729. https://doi.org/10.1016/j.tecto.2023.229729

Mohammadi, A., Ruh, J. B., Guillong, M., Laurent, O., & Aghajari, L. (2022). From Gondwana rifting to Alpine orogeny: Detrital zircon geochronologic and provenance signals from the Kopet Dagh Basin (NE Iran). *American Journal of Science*, *322*(4), 561–592. https://doi.org/10.2475/04.2022.02

Muttoni, G., Gaetani, M., Kent, D. V., Sciunnach, D., Angiolini, L., Berra, F., et al. (2009). Opening of the Neo-Tethys Ocean and the Pangea B to Pangea A transformation during the Permian. *GeoArabia*, *14*(4), 17–48. https://doi.org/10.2113/geoarabia140417

Najman, Y., Carter, A., Oliver, G., & Garzanti, E. (2005). Provenance of Eocene foreland basin sediments, Nepal: Constraints to the timing and diachroneity of early Himalayan orogenesis. *Geology*, *33*(4), 309–312. https://doi.org/10.1130/g21161.1

Negaresh, H. (2008). Mud volcanoes in Sistan and Baluchestan Provinces, Makran Coast, Southeast Iran. *Bulletin Geological Society of Malaysia*, *54*, 1–7. https://doi.org/10.7186/bgsm54200801

Nuriel, P., Wotzlaw, J.-F., Ovtcharova, M., Vaks, A., Stremtan, C., Šala, M., et al. (2021). The use of ASH-15 flowstone as a matrix-matched reference material for laser-ablation U-Pb geochronology of calcite. *Geochronology*, *3*(1), 35–47. https://doi.org/10.5194/gchron-3-35-2021

Omrani, H., Moazzen, M., Oberhansli, R., & Moslempour, M. E. (2017). Iranshahr blueschist: Subduction of the inner Makran oceanic crust. *Journal of Metamorphic Geology*, *35*(4), 373–392. https://doi.org/10.1111/jmg.12236

Pang, K. N., Chung, S. L., Zarrinkoub, M. H., Chiu, H. Y., & Li, X. H. (2014). On the magmatic record of the Makran arc, southeastern Iran: Insights from zircon U-Pb geochronology and bulk-rock geochemistry. *Geochemistry, Geophysics, Geosystems*, *15*(6), 2151–2169. https://doi.org/10.1002/2014gc005262

Pang, K. N., Chung, S. L., Zarrinkoub, M. H., Khatib, M. M., Mohammadi, S. S., Chiu, H. Y., et al. (2013). Eocene-Oligocene post-collisional magmatism in the Lut-Sistan region, eastern Iran: Magma genesis and tectonic implications. *Lithos*, *180*, 234–251. https://doi.org/10.1016/j.lithos.2013.05.009

Pang, K. N., Chung, S. L., Zarrinkoub, M. H., Mohammadi, S. S., Yang, H. M., Chu, C. H., et al. (2012). Age, geochemical characteristics and petrogenesis of Late Cenozoic intraplate alkali basalts in the Lut-Sistan region, eastern Iran. *Chemical Geology*, *306*, 40–53. https://doi.org/10.1016/j.chemgeo.2012.02.020

Perch-Nielsen, K. (1985). Mesozoic calcareous nannofossils. In H. M. Bolli, J. B. Saunders, & K. Perch-Nielsen (Eds.), *Plankton stratigraphy* (pp. 329–426). Cambridge University Press.

Platt, J. P., Leggett, J. K., Young, J., Raza, H., & Alam, S. (1985). Large-scale sediment underplating in the Makran accretionary prism, southwest Pakistan. *Geology*, *13*(7), 507–511. https://doi.org/10.1130/0091-7613(1985)13<507:lsuitm>2.0.co;2

Rad, G. R. F., Droop, G. T. R., Amini, S., & Moazzen, M. (2005). Eclogites and blueschists of the Sistan Suture Zone, eastern Iran: A comparison of P-T histories from a subduction melange. *Lithos*, *84*(1–2), 1–24. https://doi.org/10.1016/j.lithos.2005.01.007

Ricou, L. E. (1994). Tethys Reconstructed - Plates, Continental fragments and their boundaries since 260-Ma from Central-America to South-Eastern Asia. *Geodinamica Acta*, *7*(4), 169–218. https://doi.org/10.1080/09853111.1994.11105266

Roberts, N. M. W., Rasbury, E. T., Parrish, R. R., Smith, C. J., Horstwood, M. S. A., & Condon, D. J. (2017). A calcite reference material for LA-ICP-MS U-Pb geochronology. *Geochemistry, Geophysics, Geosystems*, *18*(7), 2807–2814. https://doi.org/10.1002/2016gc006784

Rossetti, F., Nasrabady, M., Vignaroli, G., Theye, T., Gerdes, A., Razavi, M. H., & Vaziri, H. M. (2010). Early Cretaceous migmatitic mafic granulites from the Sabzevar range (NE Iran): Implications for the closure of the Mesozoic peri-Tethyan oceans in central Iran. *Terra Nova*, *22*(1), 26–34. https://doi.org/10.1111/j.1365-3121.2009.00912.x

Ruh, J. B., Valero, L., Najafi, M., Etemad-Saeed, N., Vouga, J., Mohammadi, A., et al. (2023). Isotopic, fossil, sandstone petrological and paleomagnetic data from Karvandar Basin, SE Iran [Dataset]. ETH Research Collection. https://doi.org/10.3929/ethz-b-000636892

Ruh, J. B., Verges, J., & Burg, J. P. (2018). Shale-related minibasins atop a massive olistostrome in an active accretionary wedge setting: Two-dimensional numerical modeling applied to the Iranian Makran. *Geology*, *46*(9), 791–794. https://doi.org/10.1130/g40316.1

Saccani, E., Delavari, M., Dolati, A., Marroni, M., Pandolfi, L., Chiari, M., & Barbero, E. (2018). New insights into the geodynamics of Neo-Tethys in the Makran area: Evidence from age and petrology of ophiolites from the Coloured melange Complex (SE Iran). *Gondwana Research*, *62*, 306–327. https://doi.org/10.1016/j.gr.2017.07.013

Sahandi, M. R. (1996). Geological map of the Iranshahr quadrangle.

Schlunegger, F., & Castelltort, S. (2016). Immediate and delayed signal of slab breakoff in Oligo/Miocene Molasse deposits from the European Alps. *Scientific Reports*, *6*(1), 31010. https://doi.org/10.1038/srep31010

Schlunegger, F., & Kissling, E. (2015). Slab rollback orogeny in the Alps and evolution of the Swiss Molasse basin. *Nature Communications*, *6*(1), 8605. https://doi.org/10.1038/ncomms9605

Schlunegger, F., Matter, A., Burbank, D. W., & Klaper, E. M. (1997). Magnetostratigraphic constraints on relationships between evolution of the central Swiss Molasse basin and Alpine orogenic events. *Geological Society of America Bulletin*, *109*(2), 225–241. https://doi.org/10.1130/0016-7606(1997)109<0225:mcorbe>2.3.co;2

Schlunegger, F., Slingerl, R., & Matter, A. (1998). Crustal thickening and crustal extension as controls on the evolution of the drainage network of the central Swiss Alps between 30 Ma and the present: Constraints from the stratigraphy of the North Alpine Foreland Basin and the structural evolution of the Alps. *Basin Research*, *10*(2), 197–212. https://doi.org/10.1046/j.1365-2117.1998.00063.x

Senghor, A. M. C., Altiner, D., Cin, A., Ustomer, T., & Hsu, K. J. (1988). The origin and assembly of the Tethyside orogenic collage at the expense of Gondwanaland. In M. G. Audley-Charles & A. Hallam (Eds.), *Gondwana and tethys* (Vol. 37, pp. 119–181). Geological Society.

Shahabpour, J. (2010). Tectonic implications of the geochemical data from the Makran igneous rocks in Iran. *Island Arc*, *19*(4), 676–689. https://doi.org/10.1111/j.1440-1738.2010.00723.x

Sholeh, A., Rastad, E., Huston, D., Gemmell, J. B., & Taylor, R. D. (2016). The Chahnaly low-sulfidation epithermal gold deposit, western Makran volcanic arc, Southeast Iran. *Economic Geology*, *111*(3), 619–639. https://doi.org/10.2113/econgeo.111.3.619

Sinclair, H. D. (1997). Flysch to molasse transition in peripheral foreland basins: The role of the passive margin versus slab breakoff. *Geology*, *25*(12), 1123–1126. https://doi.org/10.1130/0091-7613(1997)025<1123:ftmtip>2.3.co;2

Sláma, J., Kosler, J., Condon, D. J., Crowley, J. L., Gerdes, A., Hanchar, J. M., et al. (2008). Plesovice zircon - A new natural reference material for U-Pb and Hf isotopic microanalysis. *Chemical Geology*, *249*(1–2), 1–35. https://doi.org/10.1016/j.chemgeo.2007.11.005

Spiegel, C., Kuhlemann, J., Dunkl, I., Frisch, W., von Eynatten, H., & Balogh, K. (2000). The erosion history of the Central Alps: Evidence from zircon fission track data of the foreland basin sediments. *Terra Nova*, *12*(4), 163–170. https://doi.org/10.1046/j.1365-3121.2000.00289.x

Stockmal, G. S., Beaumont, C., & Boutilier, R. (1986). Geodynamic models of convergent margin tectonics - Transition from rifted margin to overthrust belt and consequences for foreland-basin development. *Aapg Bulletin-American Association of Petroleum Geologists*, *70*(2), 181–190.

Sudi Ajirlu, M., Mohssen Moazzen, M., & Robab Hajialioghli, R. (2016). Tectonic evolution of the Zagros Orogen in the realm of the Neotethys between the Central Iran and Arabian Plates: An ophiolite perspective. *Central European Geology*, *59*(1), 1–27. https://doi.org/10.1556/24.59.2016.001

Tauxe, L., & Watson, G. S. (1994). The fold test: An eigen analysis approach. *Earth and Planetary Science Letters*, *122*(3–4), 331–341. https://doi.org/10.1016/0012-821x(94)90006-x

Tirrul, R., Bell, I. R., Griffis, R. J., & Camp, V. E. (1983). The Sistan suture zone of Eastern Iran. *Geological Society of America Bulletin*, *94*(1), 134–150. https://doi.org/10.1130/0016-7606(1983)94<134:tsszoe>2.0.co;2

Torsvik, T. H., Van der Voo, R., Preeden, U., Mac Niocaill, C., Steinberger, B., Doubrovine, P. V., et al. (2012). Phanerozoic polar wander, palaeogeography and dynamics. *Earth-Science Reviews*, *114*(3–4), 325–368. https://doi.org/10.1016/j.earscirev.2012.06.007

van der Beek, P., Robert, X., Mugnier, J. L., Bernet, M., Huyghe, P., & Labrin, E. (2006). Late Miocene–Recent exhumation of the central Himalaya and recycling in the foreland basin assessed by apatite fission-track thermochronology of Siwalik sediments, Nepal. *Basin Research*, *18*(4), 413–434. https://doi.org/10.1111/j.1365-2117.2006.00305.x

Vermeesch, P. (2018). IsoplotR: A free and open toolbox for geochronology. *Geoscience Frontiers*, *9*(5), 1479–1493. https://doi.org/10.1016/j.gsf.2018.04.001

von Quadt, A., Wotzlaw, J. F., Buret, Y., Large, S. J. E., Peytcheva, I., & Trinquier, A. (2016). High-precision zircon U/Pb geochronology by ID-TIMS using new 10(13) ohm resistors. *Journal of Analytical Atomic Spectrometry*, *31*(3), 658–665. https://doi.org/10.1039/c5ja00457h

Walker, R. T., Gans, P., Allen, M. B., Jackson, J., Khatib, M., Marsh, N., & Zarrinkoub, M. (2009). Late Cenozoic volcanism and rates of active faulting in eastern Iran. *Geophysical Journal International*, *177*(2), 783–805. https://doi.org/10.1111/j.1365-246x.2008.04024.x

Walker, R. T., & Jackson, J. (2004). Active tectonics and late Cenozoic strain distribution in central and eastern Iran. *Tectonics*, *23*(5), TC5010. https://doi.org/10.1029/2003tc001529

Wang, W. T., Zhang, P. Z., Garzione, C. N., Liu, C. C., Zhang, Z. Q., Pang, J. Z., et al. (2022). Pulsed rise and growth of the Tibetan Plateau to its northern margin since ca. 30 Ma. *Proceedings of the National Academy of Sciences of the United States of America*, *119*(8), e2120364119. https://doi.org/10.1073/pnas.2120364119

Watts, A. (1992). The effective elastic thickness of the lithosphere and the evolution of foreland basins. *Basin Research*, *4*(3–4), 169–178. https://doi.org/10.1111/j.1365-2117.1992.tb00043.x

Weissmann, G. S., Hartley, A. J., Nichols, G. J., Scuderi, L. A., Olson, M., Buehler, H., & Banteah, R. (2010). Fluvial form in modern continental sedimentary basins: Distributive fluvial systems. *Geology*, *38*(1), 39–42. https://doi.org/10.1130/g30242.1

Wiedenbeck, M., Alle, P., Corfu, F., Griffin, W. L., Meier, M., Oberli, F., et al. (1995). Three natural zircon standards for U-Th-Pb, Lu-Hf, trace-element and ree analyses. *Geostandards Newsletter*, *19*(1), 1–23. https://doi.org/10.1111/j.1751-908x.1995.tb00147.x

Young, J. R., Bown, P. R., & Lees, J. A. (2017). Nannotax3 website, international nannoplankton association. Retrieved from https://mikrotax.org/Nannotax3

Zarrinkoub, M. H., Pang, K. N., Chung, S. L., Khatib, M. M., Mohammadi, S. S., Chiu, H. Y., & Lee, H. Y. (2012). Zircon U-Pb age and geochemical constraints on the origin of the Birjand ophiolite, Sistan suture zone, eastern Iran. *Lithos*, *154*, 392–405. https://doi.org/10.1016/j.lithos.2012.08.007

Zijderveld, J. (1967). *AC demagnetization of rocks: Analysis of results, methods in paleomagnetism DW collinson, KM creer, SK Runcorn* (pp. 254–286). Elsevier.

References From the Supporting Information

Blow, W. H., & Banner, F. T. (1962). The mid-tertiary (upper Eocene to Aquitanian) Globigerinaceae. In F. E. Eames, F. T. Banner, W. H. Blow & W. J. Clarke (Eds.), *Fundamentals of mid-tertiary stratigraphical correlation* (pp. 61–151). Cambridge University Press.

Bolli, H. M. (1954). Note on Globigerina concinna Reuss 1850. *Contributions from the Cushman Foundation for Foraminiferal Research*, *5*(1), 1–3.

Bolli, H. M. (1957). Planktonic foraminifera from the Oligocene-Miocene Cipero and Lengua formations of Trinidad, BWI. *Bulletin - U.S. National Museum*, *215*, 97–131.

Bolli, H. M., Loeblich, A. R., & Tappan, H. (1957). Planktonic foraminiferal families Hantkeninidae, Orbulinidae, Globorotaliidae and Globotruncanidae. *Bulletin United States National Museum*, *215*, 3–50.

Bramlette, M. N., & Riedel, W. R. (1954). Stratigraphic value of discoasters and some other microfossils related to recent coccolithophores. *Journal of Paleontology*, *28*, 385–403.

Bramlette, M. N., & Sullivan, F. R. (1961). Coccolithophorids and related nannoplankton of the Early Tertiary in California. *Micropaleontology*, *7*(2), 129–188. https://doi.org/10.2307/1484276

Bramlette, M. N., & Wilcoxon, J. A. (1967). Middle Tertiary calcareous nannoplankton of the Cipero section, Trinidad, W.I. *Tulane Studies in Geology and Paleontology*, *5*, 93–131.

Brönnimann, P., & Stradner, H. (1960). Die Foraminiferen- und Discoasteriden-zonen von Kuba und ihre interkontinentale Korrelation. *Erdoel-Zeitschrift.*, *76*(10), 364–369.

Brotzen, F. (1936). Foraminiferen aus dem schwedischen untersten Senon von Eriksdal in Schonen. *Arsbok Sveriges Geologiska Undersökning ser. C*, *30*(3), 1–206.

Bukry, D. (1971). Cenozoic calcareous nannofossils from the Pacific Ocean. *San Diego Society of Natural History Transactions*, *16*, 303–327. https://doi.org/10.5962/bhl.part.15464

Bukry, D. (1973). Phytoplankton stratigraphy, Deep Sea Drilling Project Leg 20, Western Pacific Ocean. *Initial Reports of the Deep Sea Drilling Project*, *20*, 307–317.

Bukry, D., & Percival, S. F. (1971). New tertiary calcareous nannofossils. *Tulane Studies in Geology and Paleontology*, *8*, 123–146.

Chapman, F., Parr, W. J., & Collins, A. C. (1934). Tertiary foraminifera of Victoria, Australia.-The balcombian deposits of Port Phillip. Part III. *Journal of the Linnean Society of London: Zoology*, *38*(262), 553–577. https://doi.org/10.1111/j.1096-3642.1934.tb00996.x

Costa, O. G. (1855). Foraminiferi fossili della marna blu del Vaticano. *Memorie della Reale Accademia delle Scienze Matematiche, Scienze Naturali, e Scienze Morali*, *2*, 113–126.

Cushman, J. A. (1927). Some new genera of the Foraminifera. *Contributions from the Cushman laboratory for foraminiferal research*, *2*(4), 77–81.

Cushman, J. A., & Stainforth, R. M. (1945). *The foraminifera of the Cipero marl formation of Trinidad, British west Indies* (Vol. 14, pp. 1–75). Cushman Laboratory for Foraminiferal Research.

Deflandre, G., & Fert, C. (1954). Observations sur les coccolithophoridés actuels et fossiles en microscopie ordinaire et électronique. *Annales de Paléontologie*, *40*, 115–176.

d'Orbigny, A. D. (1846). *Die fossilen Foraminiferen des tertiären Beckens von Wien* (p. 312). Foraminifères fossiles du bassin tertiaire de Vienne.

Fornasini, C. (1885). Textularina e altri foraminiferi fossili nella marna miocenica di San Rufillo presso Bologna. *Bollettino della Societa Geologica Italiana*, *4*(1), 102–116.

Gardet, M. (1955). *Contribution à l'étude des coccolithes des terrains néogènes de l'Algérie* (Vol. 5, pp. 477–550). Publications du Service de la Carte Géologique de l'Algérie.
Hantken, M. (1868). A Kis-Czelli tályag foraminiferái (Foraminifers of the Kiscell Clay). *Magyar Földtani Társulat Munkálatai, Pest*, *4*, 75–96.
Hay, W. W., Mohler, H. P., Roth, P. H., Schmidt, R. R., & Boudreaux, J. E. (1967). Calcareous nannoplankton zonation of the Cenozoic of the Gulf Coast and Caribbean-Antillean area, and transoceanic correlation. *Transactions - Gulf Coast Association of Geological Societies*, *17*, 428–480.
Hedberg, H. D. (1937). Foraminifera of the middle tertiary carapita formation of Northeastern Venezuela. *Journal of Paleontology*, *11*, 661–697.
Howe, H. V., & Wallace, W. E. (1932). Foraminifera of the Jackson Eocene at Danville Landing on the Ouachita, Catahoula Parish, Louisiana. *Bulletin of the Geological Survey of Louisiana*, *2*, 1–118.
Jenkins, D. G. (1960). Planktonic Foraminifera from the Lakes Entrance Oil Shaft, Victoria, Australia. *Micropaleontology*, *6*(4), 345. https://doi.org/10.2307/1484217
Koch, R. E. (1926). Mitteltertiäre Foraminiferen aus Bulongan, Ost-Borneo. *Eclogae Geologicae Helvetiae*, *19*(3), 722–759.
Lamarck, J. B. P. A. (1804). Suite des mémoires sur les fossiles des environs de Paris. *Annales du Muséum d'Histoire Naturelle*, *5*.
Lipparini, T. (1932). Foraminiferi delle "Marne Azzurre" a Orbitolites e Hydrobia del Miocene superiore presso Bologna. *Giornale di Geologia*, *7*, 55–74.
Macfadyen, W. A. (1930). *Miocene foraminifera from the clysmic area of Egypt and Sinai with an account of the stratigraphy and a correlation of the local miocene succession* (pp. 1–149). Geological Survey of Egypt.
Müller, C. (1970). Nannoplankton aus dem Mittel-Oligozän von Norddeutschland und Belgien. *Neues Jahrbuch für Geologie und Paläontologie - Abhandlungen*, *135*, 82–101.
Nuttall, W. L. F. (1932). Lower Oligocene foraminifera from Mexico. *Journal of Paleontology*, *6*(1), 3–35.
Ruscelli, M. (1954). Rettifica di nomentlatura di foraminiferi per omonimia. *Rivista Italiana di Paleontologia e Stratigrafia*, *60*(4), 257.
Schiller, J. (1930). Coccolithineae. In L. Rabenhorst (Ed.), *Kryptogamen-Flora von Deutschland, Österreich und der Schweiz* (pp. 89–267). Akademische Verlagsgesellschaft.
Stradner, H. (1963). New contributions to Mesozoic stratigraphy by means of nannofossils. In *Proceedings of the sixth World petroleum congress* (pp. 167–183). Section 1 Paper 4.
Stradner, H., & Edwards, A. R. (1968). Electron microscopic studies on Upper Eocene coccoliths from the Oamaru Diatomite, New Zealand. *Jahrbuch der Geologischen Bundesanstalt*, *13*(66), 1–48.
Stradner, H., & Steinmetz, J. (1984). Cretaceous calcareous nannofossils from the Angola basin, deep sea drilling Project site 530. Initial Reports of the Deep Sea Drilling Project. (Vol. *75*, pp. 565–649).
Thalmann, H. E. (1939). Bibliography and index to new genera, species and varieties of foraminifera for the year 1936. *Journal of Paleontology*, *13*, 425–465.
von Gümbel, C. W. (1870). Beiträge zur Foraminiferenfauna der nordalpinen, älteren Eocängebilde oder der Kressenberger Nummulitenschichten. *Abhandlungen der Mathematisch-Physikalischen Klasse der Königlich Bayerischen Akademie der Wissenschaften*, *10*(2), 581–730.
Wallich, G. C. (1877). Observations on the coccosphere. *Annals and Magazine of Natural History*, *19*(112), 342–350. https://doi.org/10.1080/00222937708682153
Wise, S. W. (1973). Calcareous nannofossils from cores recovered during Leg 18, Deep Sea Drilling Project: Biostratigraphy and observations on diagenesis. *Initial Reports of the Deep Sea Drilling Project*, *18*, 569–615.